

1 **Development of East Asia Regional**
2 **Reanalysis based on advanced hybrid gain**
3 **data assimilation method and evaluation**
4 **with E3DVAR, ERA-5, and ERA-Interim**
5 **reanalysis**

6
7
8 Eun-Gyeong Yang, Hyun Mee Kim^{*}, and Dae-Hui Kim

9 *Atmospheric Predictability and Data Assimilation Laboratory*

10 *Department of Atmospheric Science, Yonsei University, Seoul, Republic of Korea*

11
12
13
14 Submitted to *Earth System Science Data*

15 June 28, 2021

16 Revision submitted on ~~March 1~~[January](#) 7, 2022

17

^{*} *Corresponding author address:* Hyun Mee Kim, Department of Atmospheric Sciences, Yonsei University, 50 Yonsei-ro, Seodaemun-gu, Seoul, 03722, Republic of Korea.

E-mail: khm@yonsei.ac.kr

18 **ABSTRACT**

19 The East Asia Regional Reanalysis (EARR) system is developed based on the advanced
20 hybrid gain data assimilation method (AdvHG) using Weather Research and Forecasting (WRF)
21 model and conventional observations. Based on EARR, the high-resolution regional reanalysis
22 and reforecast fields are produced with 12 km horizontal resolution over East Asia for 2010–
23 2019. The newly proposed AdvHG is based on the hybrid gain approach, weighting two
24 different analysis for an optimal analysis. The AdvHG is different from the hybrid gain in that
25 1) E3DVAR is used instead of EnKF, 2) 6 h forecast of ERA5 is used to be more consistent
26 with WRF, and 3) the pre-existing, state-of-the-art reanalysis is used. Thus, the AdvHG can be
27 regarded as an efficient approach to generate regional reanalysis dataset due to cost savings as
28 well as the use of the state-of-the-art reanalysis. The upper air variables of EARR are verified
29 with those of ERA5 for January and July 2017 and the ten-year period of 2010-2019. For upper
30 air variables, ERA5 outperforms EARR over two years, whereas EARR outperforms (shows
31 comparable performance to) ERA-I and E3DVAR for January in 2017 (July in 2017). EARR
32 better represents precipitation than ERA5 for January and July in 2017. Therefore, though the
33 uncertainties of upper air variables of EARR need to be considered when analyzing them, the
34 precipitation of EARR is more accurate than that of ERA5 for both two seasons. The EARR
35 data presented here can be downloaded from <https://doi.org/10.7910/DVN/7P8MZT> (Yang and
36 Kim 2021b) for data on pressure levels and <https://doi.org/10.7910/DVN/Q07VRC> (Yang and
37 Kim 2021c) for precipitation.

39 **1. Introduction**

40 Reanalysis datasets have been widely used in the socio-economical field as well as
41 meteorological and climate research areas all over the world. Most of reanalysis datasets
42 consist of global reanalysis whose spatial and temporal resolutions are relatively coarse (e.g.,
43 Schubert et al. 1993; Kalnay et al. 1996; Gibson et al. 1997; Kistler et al. 2001; Kanamitsu et
44 al. 2002; Uppala et al. 2005; Onogi et al. 2007; Bosilovich 2008; Saha et al. 2010; Dee et al.
45 2011; Rienecker et al. 2011; Bosilovich 2015; Kobayashi et al. 2015; Hersbach et al. 2020). As
46 the importance of regional reanalysis dataset emerged, many operational centers and research
47 institutes around the world have been producing the dataset in their own areas (Mesinger et al.
48 2006; Renshaw et al. 2013; Borsche et al. 2015; Bromwich et al. 2016; Jerney and Renshaw
49 2016; Zhang et al. 2017; Bromwich et al. 2018; Fukui et al. 2018; He et al. 2019; Ashrit et al.
50 2020).

51 The long-term high-resolution datasets are essential to investigate the past extreme
52 weather events which might be associated with mesoscale features such as heavy rainfall events
53 with high spatial and temporal variability which coarser-resolution model cannot represent.
54 The dynamical downscaling approaches can be a solution for generating high-resolution dataset,
55 but they have some issues with insufficient spin-up (Kayaba et al. 2016). Moreover, Fukui et
56 al. (2018) demonstrated that regional reanalysis over Japan assimilating only the conventional
57 observations had the potential to reproduce precipitation fields better than the dynamical
58 downscaling approaches. Ashrit et al. (2020) also found that the high-resolution regional
59 reanalysis over India showed substantial improvements of regional hydroclimatic features
60 during summer monsoon for the period of 1979-1993 compared to the global reanalysis ERA-
61 Interim (ERA-I, Dee et al. 2011) from ECMWF. Furthermore, He et al. (2019) revealed that
62 the pilot regional reanalysis over the Tibetan Plateau was able to represent more accurate

63 precipitation features as well as atmospheric humidity than the global reanalyses of ECMWF
64 (i.e., ECMWF's fifth-generation reanalysis (ERA5, Hersbach et al. 2020) and ERA-I).

65 As part of this effort, regional reanalysis over East Asia were produced based on the
66 Unified Model for the two-year period of 2013-2014 and it was confirmed that regional
67 reanalysis over East Asia is beneficial (Yang and Kim 2017; Yang and Kim 2019). However,
68 because UM was no longer available for generating regional reanalysis over East Asia, another
69 numerical weather prediction (NWP) model and its data assimilation (DA) method are required.

70 To find the most appropriate and cost-efficient DA method for a regional reanalysis over
71 East Asia, several DA methods were compared. Yang and Kim (2021) demonstrated that the
72 hybrid ensemble-variational data assimilation method (E3DVAR) shows the better
73 performance compared to three-dimensional variational data assimilation (3DVAR) and
74 ensemble Kalman filter (EnKF) over East Asia for January and July in 2016. However, it is
75 essential to confirm if this hybrid method is accurate enough to be used for a regional reanalysis
76 over East Asia. Thus, E3DVAR was compared with the latest and the previous reanalysis data
77 from ECMWF (ERA5 and ERA-I) for (re)analysis and (re)forecast variables and it was found
78 that a performance for a regional reanalysis needs to be further improved.

79 For this reason, a new advanced hybrid gain (AdvHG) data assimilation method, which
80 combines E3DVAR and ERA5 based on WRF model, is newly proposed and investigated in
81 this study. A hybrid gain data assimilation method has been developed as a new kind of hybrid
82 methods (Penny 2014). Based on this method, an advanced data assimilation method is newly
83 developed in this study. Finally, using this newly proposed DA method (AdvHG), East Asia
84 regional reanalysis (EARR) system is developed based on WRF model. EARR datasets have
85 been produced for ten-year period of 2010-2019 and are publicly available
86 (<https://dataverse.harvard.edu/dataverse/EARR>).

87 To investigate the accuracy and uncertainty of the state-of-the-art AdvHG DA algorithm

88 developed in this study, analysis and forecast atmospheric variables of E3DVAR, AdvHG,
89 WRF-based ERA-I, and WRF-based ERA5 are evaluated for January and July in 2017,
90 respectively. In addition, reforecast precipitation fields of ERA-I and ERA5 from ECMWF are
91 also verified and compared. In this study, the datasets are evaluated for two-month period
92 (January and July in 2017) or ten-year period (2010-2019) depending on the availability of
93 datasets. The reanalysis and (re)forecast fields of the EARR based on AdvHG and ERA5 are
94 verified for ten-year period (2010-2019). In section 2, the EARR system including model, data
95 assimilation method, and observations are explained. In section 3, the evaluation methods are
96 presented. The verification results of (re)analysis and (re)forecast variables are presented in
97 section 4. Section 4.1 presents evaluation results for wind, temperature, and humidity variables,
98 and section 4.2 presents those for precipitation (re)forecast. Section 5 presents data availability.
99 Lastly, summary and conclusions are presented in section 6.

100 **2. Reanalysis system**

101 *2.1. Model*

102 In this study, the Advanced Research Weather Research and Forecasting (WRF, v3.7.1)
103 model is used with 12-km horizontal resolution (540 x 432 grid points) and 50 vertical levels
104 (up to 5 hPa) for East Asia domain shown in Fig. 1. The model settings and physics scheme are
105 summarized in Table 1. Analysis fields are obtained every 6 h (00, 06, 12, and 18 UTC) via
106 assimilation of conventional observations with a 6 h assimilation window, and forecast fields
107 are integrated up to 36 h. The ERA5 reanalysis (Hersbach et al. 2020) is used as the first initial
108 condition before the cycling, and as boundary conditions every 6 h.

109 *2.2. Data assimilation methods*

110 *2.2.1. E3DVAR*

111 The E3DVAR method is one of hybrid data assimilation methods, which use a static

112 climatological background error covariance (BEC) and ensemble-based flow-dependent BEC,
 113 and couples the EnKF and 3DVAR (Zhang et al. 2013). E3DVAR is based on a cost function
 114 of 3DVAR. In E3DVAR, EnKF provides flow-dependent BEC as well as updates perturbations
 115 for ensemble members. Following Zhang et al. (2013),

$$J^b = J_s^b + J_e^b = \frac{1}{2} \delta \mathbf{x}^T \left[(1 - \beta) \mathbf{B} + \beta \mathbf{P}^f \circ \mathbf{C} \right]^{-1} \delta \mathbf{x} , \quad (1)$$

116 where J_s^b is a traditional cost function based on a static climatological BEC \mathbf{B} and J_e^b is an
 117 additional cost function based on ensemble-based BEC \mathbf{P}^f . \mathbf{C} is a correlation matrix for
 118 localization of the ensemble covariance \mathbf{P}^f . The weighting coefficient β between static and
 119 ensemble-based BEC is set to 0.8 in this study. To account for model error for E3DVAR, multi-
 120 physics scheme is applied to 40-member ensembles. Yang and Kim (2021) found that E3DVAR
 121 is the most appropriate DA method among 3DVAR, EnKF, and E3DVAR methods over East
 122 Asia. More detailed information on E3DVAR implemented in this study can be found in Yang
 123 and Kim (2021).

124 2.2.2. Hybrid gain data assimilation method

125 In the last decade, the traditional hybrid methods have been widely used for many
 126 operational centers and research institutes. Recently, Penny (2014) has proposed a new class
 127 of hybrid gain methods combining desirable aspects of both variational and EnKF families of
 128 algorithms by weighting analyses from 3DVAR and LETKF for an optimal analysis in the
 129 Lorenz 40-component model. Since then, this algorithm has been implemented at ECMWF
 130 (Bonavita et al. 2015) and at a hybrid global ocean DA system in National Centers for
 131 Environmental Prediction (NCEP) (Penny et al. 2015).

132 The hybrid gain algorithm can be described with the following equations:

$$\mathbf{x}_{Hyb}^a = \alpha \mathbf{x}_{det}^a + (1 - \alpha) \overline{\mathbf{x}^a} , \quad (2)$$

133 where \mathbf{x}_{Hyb}^a , \mathbf{x}_{det}^a , and $\overline{\mathbf{x}^a}$ denote the hybrid analysis, deterministic analysis, and the ensemble

134 mean analysis from the ensemble-based assimilation method, and α is a tunable parameter
 135 (Penny 2014, Houtekamer and Zhang 2016).

136 The hybrid gain method is different from traditional hybrid methods, in that a hybrid gain
 137 approach linearly combines analysis fields from EnKF and variational DA method to produce
 138 a hybrid gain analysis rather than linearly combining respective BECs (Penny 2014). Basically,
 139 the hybrid gain method is to hybridize two different Kalman gain matrices of ensemble-based
 140 [Eq. (4)] and variational data assimilation system [Eq. (5)] as in Eq. (3).

$$\hat{\mathbf{K}} = \beta_1 \mathbf{K}^f + \beta_2 \mathbf{K}^B + \beta_3 \mathbf{K}^B \mathbf{H} \mathbf{K}^f, \quad (3)$$

141 where

$$\mathbf{K}^f = \mathbf{P}^f \mathbf{H}^T (\mathbf{H} \mathbf{P}^f \mathbf{H}^T + \mathbf{R})^{-1}, \quad (4)$$

$$\mathbf{K}^B = \mathbf{B} \mathbf{H}^T (\mathbf{H} \mathbf{B} \mathbf{H}^T + \mathbf{R})^{-1}. \quad (5)$$

142 \mathbf{H} is an observation operator mapping the model state vector to observation space and \mathbf{R} is the
 143 observation error covariance matrix. The matrices \mathbf{P}^f and \mathbf{B} indicate the ensemble-based and
 144 the static climatological BEC, respectively. By choosing the specific coefficients ($\beta_1=1$, $\beta_2 =$
 145 α , $\beta_3 = -\alpha$), it can be written as in Eq. (6) and it can give an algebraically equivalent result
 146 with Eq. (2) (Penny 2014).

$$\hat{\mathbf{K}} = \mathbf{K}^f + \alpha \mathbf{K}^B (\mathbf{I} - \mathbf{H} \mathbf{K}^f). \quad (6)$$

147 One of advantages of the hybrid gain algorithm with respect to its development is that pre-
 148 existing operational systems can be used without significant modification for a hybrid analysis
 149 (Penny 2014) and independent parallel development of respective methods is allowed
 150 (Houtekamer and Zhang 2016). Furthermore, the hybrid gain approach can be considered as a
 151 practical and straightforward method in the foreseeable future to combine advantageous
 152 features of both ensemble- and variational-based DA algorithms (Houtekamer and Zhang 2016).

153 More detailed information on this algorithm can be found in Penny (2014).

154 2.2.3. *Advanced hybrid gain data assimilation method*

155 In this study, based on the hybrid gain approach, an advanced hybrid gain data assimilation
156 method (AdvHG) is newly proposed as follows:

$$X_{\text{AdvHG}}^a = \alpha X_{\text{ERA5}}^{f(6h)} + (1 - \alpha) \bar{X}_{\text{E3DVAR}}^a, \quad (7)$$

157 where $X_{\text{ERA5}}^{f(6h)}$ denotes the 6 h forecast of ERA5 reanalysis based on WRF model and $\bar{X}_{\text{E3DVAR}}^a$
158 denotes the analysis of E3DVAR (Fig. 2). In Eq. (7), α is a tunable parameter and is assigned
159 to be 0.5 in this study. This advanced hybrid gain approach is different from the hybrid gain
160 approach in that 1) E3DVAR analysis is used instead of EnKF, 2) 6 h forecast of ERA5 is used
161 instead of deterministic analysis from variational DA method, and 3) the pre-existing and state-
162 of-the-art reanalysis data (i.e., ERA5) is simply used instead of producing deterministic
163 analysis by assimilation. The reasons for these different approaches proposed in this study are
164 as follows:

165 1) E3DVAR is used instead of EnKF because Yang and Kim (2021) confirmed that
166 E3DVAR outperforms EnKF for winter and summer seasons over East Asia.

167 2) Instead of deterministic analysis, the 6 h forecast of ERA5 based on WRF model is
168 used to make the hybrid analysis more balanced and consistent with WRF model, because
169 ERA5 reanalysis fields are based on its own modeling system with coarser resolution, which
170 is different from that of this study.

171 3) European Centre for Medium-Range Weather Forecasts (ECMWF) reanalysis (ERA5)
172 is used instead of producing our own analysis fields from a variational DA method. This is a
173 very efficient approach because of the cost savings as well as the use of the high-quality latest
174 reanalysis from ECMWF assimilating all currently available observations with the state-of-the-
175 art and advanced technology.

176 Therefore, the approach proposed in this study is called as “advanced hybrid gain method”
177 (denoted as “AdvHG”).

178 2.3. Observations

179 The NCEP PrepBUFR [Prepared or QC’d data in BUFR (Binary Universal Form for the
180 Representation of meteorological data) format] conventional observations (global upper air and
181 surface weather observations, NCEP/NWS/NOAA/U.S.DOC 2008) are used every 6 h (00, 06,
182 12, and 18 UTC) for an assimilation by E3DVAR and AdvHG methods (Fig. 1). The PrepBUFR
183 is the output of the final process for preparing the observations to be assimilated in the different
184 NCEP analyses. For observations, rudimentary multi-platform quality control (QC) and more
185 complex platform-specific QC were conducted (e.g., surface pressure, rawinsonde heights and
186 temperature, wind profiler, aircraft wind and temperature) in NCEP (Keyser 2013).
187 Furthermore, if the innovations (i.e., observation minus background) of some observations are
188 greater than 5 times the observational error, then that observation is rejected during assimilation
189 procedure in this study.

190 The assimilated observations are as follows: the surface observations (SYNOP, METAR,
191 Ship, and Buoy), radiosonde observation (SOUND), upper-wind report (PILOT), wind profiler,
192 aircraft, atmospheric motion vector (AMV) wind from ~~a geostationary~~ satellites (GEOAMV),
193 and Scatterometer oceanic surface winds (Scatwind), and precipitable water vapor from global
194 positioning system (GPSPW). The observation errors depending on each observation platform,
195 variable, and vertical levels are assigned based on the default observation error statistics
196 provided in WRFDA system (Table 2). All observations are spatially thinned by 20 km except
197 for AMV thinned by 200 km as done by Warrick (2015), Cotton et al. (2016), and Shin et al.
198 (2016).

199 To evaluate 6 h accumulated precipitation simulated by E3DVAR, AdvHG, ERA-I, and
200 ERA5 over East Asia, global surface weather observations (NCEP PrepBUFR,

201 NCEP/NWS/NOAA/U.S.DOC 2008) are used every 6 h (00, 06, 12, and 18 UTC). For an
202 evaluation of the monthly precipitation fields, the world monthly surface station climatology
203 (NCDC/NESDIS/NOAA/U.S.DOC et al. 1981) over 4700 different stations (2600 in more
204 recent years) is used.

205 *2.4. Global reanalysis datasets*

206 To compare EARR generated with other reanalysis datasets, ERA5 (Hersbach et al. 2020)
207 and ERA-I (Dee et al. 2011) reanalysis are chosen. The horizontal resolutions of ERA-I and
208 ERA5 are approximately 79 km (TL255) and 31 km (TL639), respectively. Because ERA5 is
209 based on the operational system in 2016, improvements in model physics, numerics, data
210 assimilation, and additional observations over the last decade are the advantages of ERA5
211 (Hersbach et al. 2018).

212 In this study, (re)forecast as well as reanalysis fields need to be verified. Regarding
213 reanalysis and (re)forecast fields of ECMWF, reanalysis fields (i.e., ERA5 and ERA-I)
214 downloaded from ECMWF are evaluated (Figs. 3 and 6). There are two different (re)forecast
215 fields (e.g., ERA5_fromECMWF, WRF-based ERA5) used in this study. WRF-based ERA5
216 and ERA-I are forecast fields based on WRF model with 12 km horizontal resolution where
217 ERA5 and ERA-I are used as initial conditions, respectively. In contrast, ERA5_fromECMWF
218 and ERA-I_fromECMWF are reforecast fields based on ECMWF model not WRF model, so
219 the reforecast fields of ERA5 and ERA-I are provided and downloaded from ECMWF. These
220 reforecast fields are only used for evaluation of precipitation (Figs. 8 and 9). The (re)analysis
221 and (re)forecast fields and corresponding experiments are explained in Table 3.

222 **3. Evaluation method**

223 *3.1. Equitable threat score and Frequency bias index*

224 Based on the contingency table (Table 4), ETS is defined as

$$\text{ETS} = \frac{A - A_r}{A + B + C - A_r}, \text{ where } A_r = \frac{(A + B)(A + C)}{A + B + C + D}. \quad (8)$$

225 The ETS range is from -1/3 to 1 and the value 1 for ETS is a perfect score. ETS is a more
 226 balanced score than Probability of Detection (POD) and False Alarm Ratio (FAR), because it
 227 is sensitive to both false alarms and misses (Wilson 2010).

228 FBI is defined as

$$\text{FBI} = \text{Bias} = \frac{A + B}{A + C}. \quad (9)$$

229 The FBI indicates whether the model tends to over-forecast (too frequently, $\text{FBI} > 1$) or under-
 230 forecast (not frequent enough, $\text{FBI} < 1$) events with respect to frequency of occurrence.

231 3.2 Probability of detection and False alarm ratio

232 Based on the contingency table (Table 4), POD is defined as

$$\text{POD} = \frac{A}{A + C} = \frac{\text{Hits}}{\text{Hits} + \text{Misses}}. \quad (10)$$

233 The POD range is from 0 to 1. POD is required to be used with FAR, because POD can be
 234 artificially improved by systematically over-forecasting the events (Wilson 2010).

235 FAR is defined as

$$\text{FAR} = \frac{B}{A + B} = \frac{\text{False alarms}}{\text{Hits} + \text{False alarms}}. \quad (11)$$

236 The range of FAR is from 0 to 1 and its lower score implies a higher accuracy.

237 3.3 Brier skill score

238 Verification of the performance of high-resolution forecast with the traditional verification
 239 metrics (e.g., ETS, FBI) can be misleading due to double penalty, particularly for highly
 240 variable fields (e.g., precipitation). Therefore, as one of spatial verification approaches that do
 241 not require forecast to match point observation spatially, neighborhood (fuzzy) verification
 242 method, which assumes that slightly displaced forecast can be acceptable and a local

243 neighborhood can define the degree of allowable displacement (Ebert 2008; Kim et al. 2015;
 244 On et al. 2018), is used in this section. According to Ebert (2008), depending on the matching
 245 strategy, neighborhood verifications can be categorized into two frameworks: ‘single
 246 observation-neighborhood forecast (SO-NF)’ where neighborhood forecasts surrounding
 247 observations are considered, and ‘neighborhood observation-neighborhood forecast (NO-NF)’
 248 strategies where not only neighborhood forecasts but also neighborhood observations
 249 surrounding observations are considered. Due to the absence of high-resolution gridded
 250 precipitation observation data in East Asia, various verification scores widely used as
 251 ‘neighborhood observation-neighborhood forecast (NO-NF)’ strategy are not available in this
 252 study. Thus, in this section, Brier skill score as one of ‘single observation-neighborhood
 253 forecast (SO-NF)’ strategy is introduced.

254 The Brier score (BS) is similar to the mean-squared error (MSE) and is defined as (Wilks
 255 2006):

$$\text{BS} = \frac{1}{N} \sum_{i=1}^N (p_i - o_i)^2. \quad (12)$$

256 where p_i denotes the probability forecast, and o_i denotes the binary observation which is either
 257 0 or 1, and N is the total number of observations during the given period. Generally, Brier skill
 258 score (or Brier score) is used to verify ensemble forecasts which are able to calculate
 259 probabilistic forecasts (Kay et al. 2013; Kim and Kim 2017). However, Brier skill score can
 260 also be used for deterministic forecasts using a pragmatic post-processing procedure (Theis et
 261 al., 2005; Mittermaier 2014), which derives probabilistic forecasts from deterministic forecasts
 262 at every model grid point by considering neighborhood forecast as *pseudo ensemble*.

$$\text{BSS} = 1 - \frac{\text{BS}}{\text{BS}_{\text{ref}}}, \quad (13)$$

263 where BS_{ref} is Brier score of reference. Brier skill score is skill score with respect to Brier score

264 as in Eq. (13). For reference, a climatology or other forecast can be used either. In this study,
 265 the WRF-based ERA-I is considered as a reference.

266 3.4 Pattern correlation coefficient

267 The pattern correlation coefficient (PCC) is defined as Eq. (14) (Shiferaw et al. 2018; Yoo
 268 and Cho 2018; Park and Kim 2020).

$$\text{PCC} = \frac{\sum_{i=1}^N (x_i - \bar{x})(o_i - \bar{o})}{\left[\sum_{i=1}^N (x_i - \bar{x})^2 \sum_{i=1}^N (o_i - \bar{o})^2 \right]^{1/2}}, \quad (14)$$

269 where x_i and o_i are (re)forecast and observed precipitation at i th observation location and the
 270 over-bar indicates the averaged variables over N observed stations in the verification area.

271 4. Results

272 4.1 Evaluation of wind, temperature, and humidity variables

273 4.1.1 RMSE for January and July 2017

274 The analysis and forecast RMSEs of E3DVAR, AdvHG, the WRF-based ERA-I, and
 275 WRF-based ERA5 are calculated for zonal wind, meridional wind, temperature, and Qvapor
 276 (water vapor mixing ratio in WRF) variables against sonde observations at 00 and 12 UTC in
 277 verification domain (dashed box in Fig. 1) for January and July in 2017 and averaged over each
 278 month (Figs. 3, 4, and 5).

279 For analysis RMSE (Fig. 3), E3DVAR is smaller than AdvHG for all pressure levels and
 280 variables, except for temperature in July at 1000 hPa and Qvapor in January and July at 1000
 281 hPa. In general, the analysis RMSE of AdvHG for all variables is comparable to or greater than
 282 that of ERA5. The analysis RMSE of ERA5 is smaller than that of ERA-I for all levels and
 283 variables; in particular, the analysis RMSE difference between ERA5 and ERA-I is distinctive
 284 for wind.

285 Regarding wind variables of analysis (Figs. 3a, b, c, and d), E3DVAR is the most closely
286 fitted to observations except for the wind in upper troposphere in January, followed by ERA5,
287 AdvHG, and ERA-I. For temperature RMSE (Figs. 3e and f), E3DVAR is smaller than AdvHG.
288 For Qvapor, RMSE in July is much larger than that in January due to a monsoonal flow carrying
289 moist air to East Asia. In general, Qvapor RMSE of E3DVAR is the smallest, followed by
290 ERA5, AdvHG, and ERA-I. Therefore, for all variables, generally E3DVAR analysis fields are
291 the most closely fitted to observations. Since the analysis RMSE implies how much analysis
292 fields are fitted to observations rather than the accuracy of analysis itself, not only analysis
293 RMSE but also forecast RMSE should be considered.

294 For 24 h forecast fields in January (Figs. 4a, c, e, and g), overall, RMSEs of AdvHG and
295 E3DVAR are greater than those of ERA5 and smaller than those of ERA-I, and AdvHG RMSE
296 is smaller than E3DVAR RMSE for all levels and variables. Meanwhile, for July (Figs. 4b, d,
297 f, and h), AdvHG and E3DVAR show comparable RMSE to ERA-I.

298 Furthermore, general features of 36 h forecast RMSE (Fig. 5) are similar to the 24 h
299 forecast RMSE (Fig. 4). However, particularly in January, the 36 h forecast RMSE differences
300 between ERA5 and ERA-I are more distinctive compared to those of 24 h forecast. In January,
301 the vertically averaged 36 h forecast RMSE differences of ERA5 and ERA-I are 0.52 m s^{-1} for
302 wind, 0.16 K for temperature, and 0.08 g kg^{-1} for Qvapor, whereas those of 24 h forecast are
303 0.4 m s^{-1} for wind, 0.11 K for temperature, and 0.06 g kg^{-1} for Qvapor. In addition, the 36 h
304 forecast RMSE differences between ERA5 and AdvHG for January are on average 0.1 m s^{-1}
305 for wind, 0.05 K for temperature, and 0.02 g kg^{-1} for Qvapor, which are even smaller compared
306 to those of 24 h forecast, implying that AdvHG is a lot more accurate than ERA-I for January
307 in 2017. For July, 36 h forecast RMSE of ERA5 is the smallest and RMSEs of AdvHG and
308 E3DVAR are similar to those of ERA-I.

309 *4.1.2 RMSE and spread for the period of 2010-2019*

310 In this section, EARR produced in this study is verified for a longer period with WRF-
311 based ERA5. RMSE and spread of reanalyses and reforecasts based on AdvHG method are
312 calculated and averaged over the period of 2010-2019. The reanalyses and (re)forecast fields
313 are evaluated by calculating RMSE valid at 00 and 12 UTC and spread at 00, 06, 12, and 18
314 UTC.

315 The averaged RMSEs of reanalysis for ERA5 and EARR (denoted as AdvHG in Fig. 6)
316 and spread of analysis and 6 h forecast fields of EARR (AdvHG) are shown in Fig. 6. With
317 respect to spread, the ensemble spreads of analysis fields are smaller than those of 6 h forecast
318 fields, on average, by 0.15 m s^{-1} for wind, 0.04 K for temperature, and 0.02 g kg^{-1} for Qvapor,
319 which is the well-known characteristics of ensemble-based data assimilation methods. To be
320 specific, the wind spread (Figs. 6a and b) is similar to or greater than the wind RMSE except
321 for the upper troposphere above 200 hPa, implying ensemble spread for wind is well
322 represented below 200 hPa. On the contrary, the ensembles for temperature and Qvapor (Figs.
323 6c and d) are underdispersive compared to their RMSEs.

324 Regarding reanalysis RMSE, overall AdvHG RMSE is greater than ERA5 RMSE for all
325 variables (Fig. 6). The vertically averaged RMSEs of AdvHG are greater by 0.16 m s^{-1} for wind,
326 0.09 K for temperature, and 0.01 g kg^{-1} for Qvapor than those of ERA5. Nonetheless, the wind
327 RMSEs of AdvHG are similar to those of ERA5 for the middle of troposphere (400–850 hPa),
328 and the Qvapor RMSEs of AdvHG are similar to those of ERA5 except for 1000 hPa.

329 In addition, regarding 24 h forecast RMSE, AdvHG shows larger RMSE than ERA5 for
330 all variables (Fig. 7). The vertically-averaged RMSE differences of wind, temperature, and
331 Qvapor variables between AdvHG and ERA5 are approximately 0.2 m s^{-1} , 0.07 K , and 0.03 g
332 kg^{-1} , respectively. These differences are smaller, compared to the 24 h forecast RMSE
333 difference between ERA-I and ERA5 shown in Fig. 4 (i.e., wind, temperature, and Qvapor
334 RMSE difference: 0.4 m s^{-1} , 0.11 K , and 0.06 g kg^{-1} for January 2017, 0.25 m s^{-1} , 0.05 K , and

335 0.04 g kg⁻¹ for July 2017).

336 4.2 Evaluation of precipitation for January and July in 2017.

337 4.2.1 Evaluation metrics

338 4.2.1.1 Equitable threat score and Frequency bias index

339 In this section, for the point-based Equitable threat score (ETS) and Frequency bias index
340 (FBI) based on Table 4, the 6 h accumulated precipitation fields based on the 6 h forecast of
341 E3DVAR, AdvHG, WRF-based ERA-I, WRF-based ERA5, ERA-I_fromECMWF, and
342 ERA5_fromECMWF are evaluated every 6 h (00, 06, 12, and 18 UTC) for January and July in
343 2017 (Fig. 8). Here, all the WRF-based precipitation fields are based on 12-km horizontal
344 resolution, and ERA-I_fromECMWF and ERA5_fromECMWF have 79- and 31-km horizontal
345 resolutions, respectively. Generally, ETS decreases as a threshold increases for both two
346 months (Figs. 8a and c). For January in 2017 (Fig. 8a), AdvHG ETS is the greatest among
347 others. Compared to precipitation reforecasts from ECMWF (i.e., ERA-I_fromECMWF,
348 ERA5_fromECMWF), AdvHG shows the higher ETS, indicating that AdvHG is able to
349 simulate more accurate precipitation fields than ERA-I and ERA5 from ECMWF in January
350 2017. Surprisingly, ETS of ERA5_fromECMWF for January in 2017 is the lowest among all
351 the results compared and is even lower than that of ERA-I_fromECMWF.

352 Since the precipitation reforecasts from ECMWF have not only coarser resolutions but
353 also different forecast model (i.e., the forecasting system of ECMWF), the precipitation
354 forecasts of ERA5 and ERA-I are additionally produced by using the same forecast model with
355 the same resolution as AdvHG and E3DVAR in this study, as explained in section 2.4. For
356 January 2017 (Fig. 8a), ETS of ERA5 (i.e., WRF-based ERA5) is higher than that of
357 ERA5_fromECMWF for all thresholds, whereas ETS of ERA-I (i.e., WRF-based ERA-I) is
358 lower than that of ERA-I_fromECMWF except for high thresholds (8 and 16 mm (6 h)⁻¹). The
359 ERA5 ETS is greater than the ERA-I ETS, but is smaller than the AdvHG ETS. The AdvHG

360 shows the greatest ETS among others with the same resolution and forecast model, and
361 E3DVAR, ERA5, and ERA-I follow.

362 Regarding FBI in winter (Fig. 8b), for 4, 8, and 16 mm (6 h)⁻¹ thresholds, all the results
363 show the FBI smaller than 1, implying the underestimation of frequency of precipitation for
364 high-threshold events. In general, AdvHG shows the FBI closest to 1 among all the results,
365 which is consistent with the greatest ETS of AdvHG. The E3DVAR FBI is similar to the
366 AdvHG FBI, and ERA5 and ERA-I FBIs are similar to each other.

367 Meanwhile, overall, the ETS values for January whose maximum is around 0.4 (Fig. 8a)
368 are much greater than those for July in 2017 whose maximum is around 0.2 (Fig. 8c), implying
369 that the precipitation forecast in summer is more difficult than that in winter. The ETS
370 difference between the results in July is smaller than those in January. Particularly, for the
371 thresholds 4 and 8 mm (6 h)⁻¹, ETSs in July are similar to each other (Fig. 8c). Except for those
372 two thresholds, the ETS of ERA-I_fromECMWF is the smallest. At the threshold 16 mm (6 h)
373 ⁻¹, ERA5 ETS is the highest, followed by AdvHG, E3DVAR, ERA-I, ERA5_fromECMWF, and
374 ERA-I_fromECMWF. At the threshold 0.5 and 1 mm (6 h)⁻¹, the E3DVAR ETS is the greatest,
375 followed by ERA5, AdvHG, ERA5_fromECMWF, ERA-I, and ERA-I_fromECMWF.

376 With respect to FBI in July 2017, the WRF-based results show the FBIs greater than 1,
377 whereas reforecast from ECMWF show the FBIs greater than 1 for 0.5, 1, and 4 mm (6 h)⁻¹
378 thresholds and smaller than 1 for higher thresholds (8 and 16 mm (6 h)⁻¹) (Fig. 8d). For July in
379 2017, in general, ERA5_fromECMWF FBI is the closest to 1, followed by E3DVAR, AdvHG,
380 ERA5, ERA-I, and ERA-I_fromECMWF FBI.

381 *4.2.1.2 Probability of detection and False alarm ratio*

382 The Probability of Detection (POD or Hit Rate) and False Alarm Ratio (FAR) are
383 calculated for precipitation simulated from E3DVAR, AdvHG, WRF-based ERA-I, WRF-
384 based ERA5, ERA-I_fromECMWF, and ERA5_fromECMWF for January and July in 2017

385 (Fig. 9). For January in 2017, AdvHG POD is the greatest among the WRF-based results,
386 followed by E3DVAR, ERA5, and ERA-I (Fig. 9a). In addition to the lowest ETS of
387 ERA5_fromECMWF for January in 2017 as discussed in the section 4.2.1.1, FAR of
388 ERA5_fromECMWF is extremely high with low POD in winter. Therefore, especially for
389 January in 2017, the precipitation fields simulated from EARR (AdvHG) over East Asia are a
390 lot more accurate than those from ERA5_fromECMWF.

391 For July in 2017, generally, AdvHG shows the largest POD, except for ERA5 (Fig. 9c).
392 With respect to FAR, FAR values in July are much greater than those in January, which is
393 consistent with the ETS difference between these two seasons.

394 *4.2.1.3 Brier skill score*

395 The neighborhood sizes are chosen to be $3\Delta x$, $5\Delta x$, $9\Delta x$, and $11\Delta x$, which are 36, 60,
396 108, and 132 km, respectively, and the thresholds 0.5, 1, 4, 8, and 16 mm (6 h)⁻¹ are considered.
397 The probabilistic precipitation forecasts are calculated at every model grid point depending on
398 neighborhood sizes and thresholds. Regarding each observation, the nearest model grid point
399 to observations is considered as the center of neighborhood. For verification, 6 h accumulated
400 precipitation fields are extracted from the first 0–6 h forecast fields of WRF-based ERA-I,
401 WRF-based ERA5, E3DVAR, and AdvHG every 6 h (00, 06, 12, and 18 UTC). BSSs of
402 ERA5_fromECMWF and ERA-I_fromECMWF are not calculated, because they have different
403 resolution from WRF-based results.

404 Based on the neighborhood approach, Brier skill score (BSS) is calculated depending on
405 different neighborhood sizes for January and July in 2017, respectively (Fig. 10). Because the
406 reference of Brier score is chosen as the ERA-I, the positive BSS implies better accuracy than
407 ERA-I. In general, for both two months, AdvHG BSS is greater than ERA5 BSS. Although the
408 E3DVAR BSS is the greatest in July 2017, the AdvHG BSS is the greatest in January 2017.

409 For January in 2017, as a neighborhood size increases, AdvHG and E3DVAR BSSs tend

410 to increase except for ERA5. Overall, AdvHG BSS is the greatest among other BSSs for all
411 thresholds for all neighborhood sizes. The ERA5 BSS is greater than E3DVAR BSS except for
412 16 mm (6 h)⁻¹. The highest BSS of AdvHG and the lowest BSS of ERA-I are consistent with
413 ETS result. Unlike greater E3DVAR ETS than ERA5 ETS, ERA5 BSS is greater than E3DVAR
414 BSS in January 2017.

415 For July 2017, while the ETS difference between the WRF-based results is not distinct
416 (Fig. 8c), the BSS difference is rather noticeable. Generally, E3DVAR BSS is the greatest
417 among other BSSs for all thresholds except for 16 mm (6 h)⁻¹ for neighborhood sizes 9 and 11.
418 Although E3DVAR BSS is the largest, AdvHG outperforms ERA5 and ERA-I. The worst
419 performance of ERA-I precipitation is consistent with ETS result. At 0.5, 1, and 4 mm (6 h)⁻¹
420 thresholds, E3DVAR BSS is the greatest, which is similar to ETS. At 8 and 16 mm (6 h)⁻¹
421 thresholds, ERA5 ETS is the highest, followed by AdvHG and E3DVAR, whereas overall
422 E3DVAR BSS is the highest, followed by AdvHG and ERA5.

423 4.2.2 *Spatial distribution*

424 4.2.2.1 *6 h accumulated precipitation with the pattern correlation coefficient*

425 In this section, the spatial distributions of 6 h accumulated precipitation from the WRF-
426 based forecast and reforecast from ECMWF are compared. In addition, pattern correlation
427 coefficients (PCC) are calculated and shown at the bottom right of Figs. 11 and 12.

428 The PCC is computed according to the usual Pearson correlation operating on the N
429 observed point pairs of 6 h accumulated precipitation fields simulated from (re)forecast and
430 observations at the specific time. For the calculation of PCC, 6 h accumulated precipitation
431 fields from (re)forecast fields are interpolated bilinearly to the N observed points.

432 Firstly, on 29th and 30th of January in 2017 (Fig. 11), it is noticeable that the precipitation
433 fields of AdvHG match observations well over East Asia, whereas, in particular, those of
434 ERA5_fromECMWF do not. For example, ERA5_fromECMWF overestimates precipitation

435 over inland area of China (Fig. 11zz), while AdvHG simulates precipitation similar to
436 observations regarding its position and intensity (Fig. 11x). ERA5_fromECMWF also shows
437 noticeably smaller PCC (Figs. 11g, n, and zz). Although PCC does not represent the exact
438 accuracy or predictability of precipitation, the overall feature of PCC is consistent with the
439 results found so far. For January in 2017, the averaged PCC of AdvHG is the greatest (i.e., 0.61)
440 and that of ERA5_fromECMWF is the smallest (i.e., 0.46) (not shown).

441 For 1st and 2nd of July in 2017 (Fig. 12), in general, AdvHG, E3DVAR, and ERA5 well
442 simulate not only overall features of precipitation fields but also their intensity. During July in
443 2017, ERA5 and ERA-I simulate heavier precipitation than AdvHG (not shown), which is
444 consistent with larger FBI of ERA5 and ERA-I at higher thresholds. For one-month period of
445 July in 2017, the averaged PCC of ERA5 is the greatest (i.e., 0.37) and that of AdvHG is 0.34,
446 but the PCC difference between ERA5 and AdvHG is not distinctive. Moreover, the overall
447 range of averaged PCC of different datasets in summer (i.e., 0.29-0.35) is smaller than that in
448 winter (i.e., 0.46-0.61), which is consistent with the seasonal difference of ETS in this study.

449 4.2.2.2 *Monthly accumulated precipitation*

450 In this section, the monthly accumulated precipitation fields of rain gauge based
451 observations, E3DVAR, AdvHG, ERA-I, ERA5, ERA-I_fromECMWF, and
452 ERA5_fromECMWF are compared to each other for two one-month periods in January and
453 July in 2017, respectively.

454 The monthly accumulated precipitation fields simulated by E3DVAR and AdvHG (Figs.
455 13b and c) are similar to each other, and E3DVAR and AdvHG produce the best fit to observed
456 fields. Especially, for the north-western part of Japan (e.g., Chugoku and Kinki), E3DVAR and
457 AdvHG are able to represent precipitation correctly, whereas ERA-I_fromECMWF and
458 ERA5_fromECMWF fail to do so (Fig. 13). Moreover, although all the results similarly
459 represent overall features of precipitation in January (Fig. 13), ERA5_fromECMWF (Fig. 13g)

460 simulates the overestimated precipitation over South China, which is consistent with the results
461 in the previous section as well as its larger FBI at lower thresholds (0.5 and 1 mm (6 h)^{-1}) shown
462 in Fig. 8b. It is noticeable that all results fail to represent the observed precipitation area over
463 Tibetan Plateau (25° – 40° N, 95° – 105° E).

464 For the monthly accumulated precipitation in July 2017, overall, the ERA5_fromECMWF
465 (Fig. 14g) and the WRF-based results (Figs. 14b, c, and e) except for ERA-I (Fig. 14d) well
466 simulate precipitation similar to observations. The WRF-based results including AdvHG
467 overestimate precipitation over western and southern part of Japan, while ERA-
468 I_fromECMWF and ERA5_fromECMWF simulate similar precipitation fields to observed
469 fields. The WRF-based results tend to overestimate precipitation in South China, Korea, and
470 Japan, compared to ERA-I_fromECMWF and ERA5_fromECMWF. This is consistent with
471 the result in Fig. 8d, in which FBIs from WRF-based results are generally greater than for
472 higher thresholds (8 and 16 mm (6 h)^{-1}), whereas those from ECMWF are smaller than 1.

473 Even though detailed precipitation features of WRF-based results are different, overall
474 features of precipitation from WRF-based results are similar to each other, which implies that
475 predictability of precipitation strongly depends on the physics schemes as well as NWP model,
476 especially for summer season. According to Que et al. (2016), depending on the combinations
477 of physics options in WRF model, the spatial distribution of precipitation can be significantly
478 different over Asian summer monsoon area and YSU PBL scheme which is used in this study
479 tends to overestimate precipitation over the same area. Thus, different physics options could
480 simulate the different spatial distribution of precipitation.

481 In addition, compared to ERA5 based on WRF model (Fig. 14e), ECMWF model for
482 ERA5_fromECMWF (Fig. 14g) seems to suppress precipitation. Thus, WRF model with the
483 physics schemes used in this study might simulate more precipitation than ECMWF model,
484 although the initial condition is the same. Therefore, it is important to consider the consistency

485 of the systems for data assimilation and forecast model for a good performance of forecast
486 weather variables like precipitation.

487 **5. Data Availability**

488 The EARR data presented in this study are available every 6 h (i.e., 00, 06, 12, and 18
489 UTC) for the period of 2010-2019 from Harvard Dataverse Repository
490 (<https://dataverse.harvard.edu/dataverse/EARR>). The EARR 6 hourly data on pressure levels
491 (<https://doi.org/10.7910/DVN/7P8MZT>, Yang and Kim 2021b) and 6 hourly precipitation data
492 (<https://doi.org/10.7910/DVN/Q07VRC>, Yang and Kim 2021c) are provided in NetCDF file
493 format.

494 The EARR 6 hourly data on pressure levels (Yang and Kim 2021b) include u-component
495 of wind, v-component of wind, temperature, geopotential height, and specific humidity
496 variables of reanalysis on pressure levels (i.e., 925, 850, 700, 500, 300, 200, 100, and 50 hPa).
497 The EARR 6 hourly precipitation data (Yang and Kim 2021c) contain 6 h accumulated total
498 precipitation variable of 6 h reforecast on single level. The 6 h accumulated total precipitation
499 is obtained from 6 h reforecast field which is integrated for 6 h from reanalysis field every 6 h
500 (i.e., 00, 06, 12 and 18 UTC).

501 **6. Summary and conclusions**

502 In this study, to develop the regional reanalysis system over East Asia, the advanced
503 hybrid gain algorithm (AdvHG) is newly proposed and evaluated with traditional hybrid DA
504 method (E3DVAR) as well as existing reanalyses from ECMWF (ERA5 and ERA-I) for
505 January and July in 2017. The East Asia Regional Reanalysis (EARR) system is developed
506 based on the AdvHG as the data assimilation method using WRF model and conventional
507 observations. The high-resolution regional reanalysis and reforecast fields over East Asia with
508 12 km horizontal resolution are produced and evaluated against observations with ERA5 for

509 the ten-year period of 2010–2019.

510 The AdvHG newly proposed in this study is based on the hybrid gain approach, weighting
511 analyses from variational-based and ensemble-based DA algorithms to generate optimal hybrid
512 analysis, which can play an important role as a simple and practical method in the foreseeable
513 future to take advantage of each strength of two different DA methods. The advanced hybrid
514 gain method is different from the hybrid gain approach in that 1) E3DVAR is used instead of
515 EnKF, 2) 6 h forecast of ERA5 is used instead of deterministic analysis for a more balanced
516 and consistent analysis with WRF model, and 3) the pre-existing and state-of-the-art reanalysis
517 data (i.e. ERA5) is simply used instead of producing our own analysis fields from a variational
518 DA method. Thus, it can be regarded as an efficient approach to generate regional reanalysis
519 dataset because of cost savings as well as the use of the state-of-the-art reanalysis from
520 ECMWF that assimilates all available observations.

521 For a verification, the latest ECMWF reanalysis and reforecast datasets (i.e., ERA5 and
522 ERA-I) are used. With respect to forecast variables, two different forecast fields of ECWMF
523 are used: 1) reforecast fields from ECMWF (i.e., ERA5_fromECMWF and ERA-
524 I_fromECMWF) and 2) forecast fields (i.e., WRF-based ERA5 and WRF-based ERA-I)
525 integrated in WRF model with 12 km resolution using ERA5 and ERA-I as initial conditions.

526 Analysis and forecast wind, temperature, and humidity variables of AdvHG are evaluated
527 with ERA5 for the ten-year period and evaluated with five different experiments (i.e., E3DVAR,
528 ERA5, ERA-I, ERA5_fromECMWF, ERA-I_fromECMWF) for January and July in 2017.
529 Overall, the analysis RMSE of E3DVAR is the smallest among others but comparable to that
530 of ERA5, especially for January in 2017. Regarding forecast variables, AdvHG outperforms
531 E3DVAR for January and July in 2017. Although ERA5 outperforms AdvHG for upper air
532 variables for two seasons in 2017, AdvHG outperforms ERA-I in January and shows
533 comparable performance to ERA-I in July. Additionally the verification results of AdvHG and

534 ERA5 for the period of 2010-2019 are consistent with those for two one-month period in 2017.

535 The precipitation forecast variables are also verified regarding a neighborhood-based
536 verification score (i.e., Brier skill score) as well as the point-based verification scores (i.e., ETS,
537 FBI, POD, and FAR). According to the point-based verification scores, the precipitation
538 forecast of AdvHG in January is the most accurate, followed by E3DVAR, ERA5, ERA-I. For
539 July, overall ETS values of all results are relatively lower compared to those in January,
540 implying the lower predictability in summer season. In addition, the ETS differences between
541 the results are not distinctive in July. For higher thresholds (8 and 16 mm (6 h)⁻¹) in July,
542 AdvHG ETS is greater than E3DVAR ETS and smaller than ERA5 ETS, whereas E3DVAR
543 ETS is the greatest followed by ERA5 and AdvHG for lower thresholds (0.5 and 1 mm (6 h)⁻¹).
544 ¹).

545 To prevent from double penalty when verifying a highly variable data with high resolution
546 (e.g., precipitation), Brier skill score (BSS) based on neighborhood approach is calculated for
547 6 h accumulated precipitation forecasts depending on different neighborhood sizes for January
548 and July in 2017. In general, BSS of AdvHG is greater than that of ERA5 and ERA-I for both
549 two months. Although the E3DVAR BSS is the greatest in July 2017, the AdvHG BSS is the
550 greatest in January 2017.

551 Lastly, the spatial distributions of 6 h and monthly accumulated precipitation forecast for
552 AdvHG, E3DVAR, ERA-I, ERA5, ERA-I_fromECMWF, and ERA5_fromECMWF are
553 compared with rain-gauge based observations. For January 2017, it is noticeable that AdvHG
554 precipitation is the closest to observations with highest PCC (i.e., 0.61) and
555 ERA5_fromECMWF overestimates precipitation over South China with the lowest PCC (i.e.,
556 0.46). For July in 2017, the WRF-based results tend to overestimate precipitation compared to
557 ERA-I_fromECMWF and ERA5_fromECMWF. In addition, even though the averaged PCC
558 of ERA5 (i.e., 0.37) is slightly greater than that of AdvHG (i.e., 0.34), the PCC difference

559 between ERA5 and AdvHG is not distinctive and overall range of averaged PCC of all datasets
560 in summer (i.e., 0.29-0.37) is smaller than that in winter (i.e., 0.46-0.6).

561 In conclusion, for upper air variables, overall, ERA5 outperforms EARR based on AdvHG,
562 but the RMSE difference between ERA5 and EARR (AdvHG) is smaller than that between
563 ERA5 and ERA-I. In addition, EARR outperforms ERA-I for January 2017 and shows
564 comparable performance to ERA-I for July 2017. On the contrary, according to the evaluation
565 results of precipitation, in general, EARR better represents precipitation than ERA5 as well as
566 ERA5_fromECMWF for January and July in 2017. Even if E3DVAR precipitation is better
567 represented than EARR precipitation for July, the difference is not considerable for July and
568 EARR better simulates precipitation for January than E3DVAR. Therefore, although the
569 uncertainties of upper air variables of EARR should be considered when analyzing them, the
570 precipitation reforecast of EARR is more accurate than that of ERA5 for both two seasons.

571 Combining the global reanalysis data (i.e., ERA5) characterized by the high quality of
572 large-scale features with detailed smaller-scale features in the higher resolution represented by
573 ensemble-based assimilation method (i.e., E3DVAR) as well as a community numerical
574 weather prediction model (i.e., WRF model) is a key factor of EARR to be able to produce
575 high-resolution initial conditions represented with regional features, which could contribute to
576 reduction of forecast errors, especially for precipitation. Therefore, EARR has its own
577 advantage of representing regional features of precipitation better than relatively coarse-
578 resolution global reanalysis.

579

580 **Author contribution**

581 Hyun Mee Kim proposed the main scientific ideas and Eun-Gyeong Yang contributed the
582 supplementary ideas during the process. Eun-Gyeong Yang developed the reanalysis system
583 and produced the 10-year regional reanalysis data. Eun-Gyeong Yang and Hyun Mee Kim

584 analyzed the simulation results and completed the manuscript. Dae-Hui Kim contributed to
585 analyzing the reanalysis data and to the preparation of software and computing resources for
586 the reanalysis system.

587

588 **Competing interests**

589 The authors declare that they have no competing interests.

590

591 **Acknowledgments**

592 The authors appreciate reviewers for their valuable comments. This study was supported by a
593 National Research Foundation of Korea (NRF) grant funded by the South Korean government
594 (Ministry of Science and ICT) (Grant 2021R1A2C1012572) and the Yonsei Signature Research
595 Cluster Program of 2021 (2021-22-0003). This study was carried out by utilizing the
596 supercomputer system supported by the National Center for Meteorological Supercomputer of
597 Korea Meteorological Administration and Korea Research Environment Open NETWORK
598 (KREONET) provided by the Korea Institute of Science and Technology Information. The
599 authors gratefully acknowledge the late Dr. Fuqing Zhang for collaborations at the earlier
600 stages of this study.

601

602

603 **References**

- 604 Ashrit, R., S. Indira Rani, S. Kumar, S. Karunasagar, T. Arulalan, T. Francis, A. Routray, S. I. Laskar,
605 S. Mahmood, P. Jerney, A. Maycock, R. Renshaw, J. P. George, and E. N. Rajagopal, 2020:
606 IMDAA Regional Reanalysis: Performance Evaluation During Indian Summer Monsoon
607 Season. *Journal of Geophysical Research: Atmospheres*, **125**(2), e2019JD030973.
- 608 Bonavita, M., M. Hamrud, and L. Isaksen, 2015: EnKF and hybrid gain ensemble data assimilation.
609 Part II: EnKF and hybrid gain results. *Monthly Weather Review*, **143**(12), 4865-4882.
- 610 Borsche, M, A. K. Kaiser-Weiss, P. Undén, and F. Kaspar, 2015: Methodologies to characterize
611 uncertainties in regional reanalyses. *Adv. Sci. Res.*, **12**, 207-218.
- 612 Bosilovich, M., 2008: NASA's modern era retrospective-analysis for research and applications:
613 Integrating Earth observations. Earthzine, 26 September 2008. [Available online at
614 www.earthzine.org/2008/09/26/nasas-modern-era-retrospective-analysis/.]
- 615 Bosilovich, M., R. Lucchesi, and M. Suarez, 2015: MERRA-2: File specification. NASA GMAO Office
616 Note 9, 73 pp., <http://gmao.gsfc.nasa.gov/pubs/docs/Bosilovich785.pdf>.
- 617 Bromwich, D. H., A. B. Wilson, L. Bai, Z. Liu, M. Barlage, C. F. Shih, S. Maldonado, K. M. Hines, S.-
618 H. Wang, J. Woollen, B. Kuo, H.-C. Lin, T.-K. Wee, M. C. Serreze, and J. E. Walsh, 2018: The
619 Arctic system reanalysis, version 2. *Bulletin of the American Meteorological Society*, **99**(4),
620 805-828.
- 621 Bromwich, D. H., A. B. Wilson, L. S. Bai, G. W. Moore, and P. Bauer, 2016: A comparison of the
622 regional Arctic System Reanalysis and the global ERA-Interim Reanalysis for the Arctic.
623 *Quarterly Journal of the Royal Meteorological Society*, **142**(695), 644-658.
- 624 Cotton, J., M. Forsythe, F. Warrick, K. Salonen, N. Bormann, and K. Lean, 2016: AMVs in the Tropics:
625 use in NWP, data quality and impact, Joint ECMWF/ESA Workshop on 'Tropical modeling,
626 observations and data assimilation [Available online at <https://www.ecmwf.int/node/16865>]
- 627 Dee, D. P., S. M. Uppala, A. J. Simmons, P. Berrisford, P. Poli, S. Kobayashi, U. Andrae, M. A.
628 Balmaseda, G. Balsamo, P. Bauer, P. Bechtold, A. C. M. Beljaars, L. van de Berg, J. Bidlot, N.
629 Bormann, C. Delsol, R. Dragani, M. Fuentes, A. J. Geer, L. Haimberger, S. B. Healy, H.

630 Hersbach, E. V. Hólm, L. Isaksen, P. Kållberg, M. Köhler, M. Matricardi, A. P. McNally, B. M.
631 Monge-Sanz, J.-J. Morcrette, B.-K. Park, C. Peubey, P. de Rosnay, C. Tavalato, J.-N. Thépaut,
632 and F. Vitart, 2011: The ERA-Interim reanalysis: configuration and performance of the data
633 assimilation system. *Q. J. R. Meteorol. Soc.*, **137**, 553–597. doi: 10.1002/qj.828

634 Ebert, E. E., 2008: Fuzzy verification of high-resolution gridded forecasts: a review and proposed
635 framework. *Meteorological Applications: A journal of forecasting, practical applications,*
636 *training techniques and modelling*, **15**(1), 51-64.

637 Fukui, S., T. Iwasaki, K. Saito, H. Seko, and M. Kunii, 2018: A feasibility study on the high-resolution
638 regional reanalysis over Japan assimilating only conventional observations as an alternative to
639 the dynamical downscaling. *Journal of the Meteorological Society of Japan*. **96**(6), 565-585.

640 Gibson, J. K., P. Kållberg, S. Uppala, A. Nomura, A. Hernandez, E. Serrano, 1997: ERA Description.
641 *ECMWF Re-Analysis Final Report Series*, **1**, 71pp.

642 Grell, G. A., and S. R. Freitas, 2014: A scale and aerosol aware stochastic convective parameterization
643 for weather and air quality modeling. *Atmos. Chem. Phys*, **14**(10), 5233-5250.

644 He, J., F. Zhang, X. Chen, X. Bao, D. Chen, H. M. Kim, H.-W. Lai, L. R. Leung, X. Ma, Z. Meng, T.
645 Ou, Z. Xiao, E.-G. Yang, and K. Yang, 2019: Development and evaluation of an ensemble-based
646 data assimilation system for regional reanalysis over the Tibetan Plateau and surrounding
647 regions, *Journal of Advances in Modeling Earth Systems*, **11**(8), 2503-2522.

648 Hersbach, H., B. Bell, P. Berrisford, S. Hirahara, A. Horányi, J. Muñoz-Sabater, J. Nicolas, C. Peubey,
649 R. Radu, D. Schepers, A. Simmons, C. Soci, S. Abdalla, X. Abellan, G. Balsamo, P. Bechtold,
650 G. Biavati, J. Bidlot, M. Bonavita, G. D. Chiara. P. Dahlgren, D. Dee, M. Diamantakis, R.
651 Dragani, J. Flemming, R. Forbes, M. Fuentes, A. Geer, L. Haimberger, S. Healy, R. J. Hogan, E.
652 Hólm, M. Janisková, S. Keeley, P. Laloyaux, P. Lopez, C. Lupu, G. Radnoti, P. de Rosnay, I.
653 Rozum, F. Vamborg, S. Villaume, and J.-N. Thépaut, 2020: The ERA5 global reanalysis.
654 *Quarterly Journal of the Royal Meteorological Society*, **146**(730), 1999-2049.

655 Hersbach, H., P. de Rosnay, B. Bell, D. Schepers, A. Simmons, C. Soci, S. Abdalla, M. Alonso
656 Balmaseda, G. Balsamo, P. Bechtold, P. Berrisford, J. Bidlot, Eric. de Boissésou, M. Bonavita,

657 P. Browne, R. Buizza, P. Dahlgren, D. Dee, R. Dragani, M. Diamantakis, J. Flemming, R. Forbes,
658 A. Geer, T. Haiden, E. Hólm, L. Haimberger, R. Hogan, A. Horányi, M. Janisková, P. Laloyaux,
659 P. Lopez, J. Muñoz-Sabater, C. Peubey, R. Radu, D. Richardson, J.-N. Thépaut, F. Vitart, X.
660 Yang, E. Zsótér, and H. Zuo, 2018: Operational global reanalysis: progress, future directions
661 and synergies with NWP, *ECMWF ERA report series*, N27.

662 Hong, S.-Y., Y. Noh, and J. Dudhia, 2006: A new vertical diffusion package with an explicit treatment
663 of entrainment processes. *Monthly Weather Review*, **134**(9), 2318-2341.

664 Houtekamer, P. L., and F. Zhang, 2016: Review of the ensemble Kalman filter for atmospheric data
665 assimilation. *Monthly Weather Review*, **144**(12), 4489-4532.

666 Iacono, M. J., J. S. Delamere, E. J. Mlawer, M. W. Shephard, S. A. Clough, and W. D. Collins, 2008:
667 Radiative forcing by long-lived greenhouse gases: Calculations with the AER radiative transfer
668 models. *Journal of Geophysical Research: Atmospheres*, **113**(D13).

669 Jerney, P. M., and R. J. Renshaw, 2016: Precipitation representation over a two-year period in regional
670 reanalysis. *Q. J. R. Meteorol. Soc.*, **142**, 1300-1310.

671 Jiménez, P. A., J. Dudhia, J. F. González-Rouco, J. Navarro, J. P. Montávez, and E. García-Bustamante,
672 2012: A revised scheme for the WRF surface layer formulation. *Mon. Wea. Rev.*, **140**(3), 898-
673 918.

674 Kayaba, N., T. Yamada, S. Hayashi, K. Onogi, S. Kobayashi, K. Yoshimoto, K. Kamiguchi, and K.
675 Yamashita, 2016: Dynamical regional downscaling using the JRA-55 reanalysis (DSJRA-55).
676 *Sola*, **12**, pp.1-5.

677 Kalnay, E., M. Kanamitsu, R. Kistler, W. Collins, D. Deaven, L. Gandin, M. Iredell, S. Saha, G. White,
678 J. Woolen, Y. Zhu, M. Chelliah, W. Ebisuzaki, W. Higgins, J. Janowiak, K. C. Mo, C. Ropelewski,
679 J. Wang, A. Leetmaa, R. Reynolds, Roy Jenne and Dennis Joseph, 1996: The NCEP/NCAR 40-
680 year reanalysis project. *Bull. Amer. Meteorol. Soc.*, **77**, 437-471.

681 Kanamitsu, M., W. Ebisuzaki, J. Woollen, S.-K. Yang, J. J. Hnilo, M. Fiorino, and G. L. Potter, 2002:
682 NCEP–DOE AMIP-II Reanalysis (R-2). *Bull. Amer. Meteor. Soc.*, **83**, 1631–1643.

683 Kay, J. K., H. M. Kim, Y.-Y. Park, and J. Son, 2013: Effect of doubling ensemble size on the

684 performance of ensemble prediction in warm season using MOGREPS implemented in
685 KMA, *Advances in Atmospheric Sciences*, **30**(5), 1287-1302, doi:10.1007/s00376-012-2083-y.

686 Keyser, D., 2013: An Overview of Observational Data Processing at NCEP (with information on BUFR
687 Format including “PrepBUFR” files), *GSI tutorial*, August 6, 2013.

688 Kim, S., H. M. Kim, J. K. Kay, and S.-W. Lee, 2015: Development and evaluation of high resolution
689 limited area ensemble prediction system in KMA, *Atmosphere*, 25(1), 67-83. (in Korean with
690 English abstract)

691 Kim, S., and H. M. Kim, 2017: Effect of considering sub-grid scale uncertainties on the forecasts of a
692 high-resolution limited area ensemble prediction system, *Pure and Applied Geophysics*, **174**(5),
693 2021-2037, doi: 10.1007/s00024-017-1513-2.

694 Kistler, R., W. Collins, S. Saha, G. White, J. Woollen, E. Kalnay, M. Chelliah, W. Ebisuzaki, M.
695 Kanamitsu, V. Kousky, H. v. d. Dool, R. Jenne, and M. Fiorino, 2001: The NCEP–NCAR 50–
696 Year Reanalysis: Monthly Means CD–ROM and Documentation. *Bull. Amer. Meteor. Soc.*, **82**,
697 247–267.

698 Kobayashi, S., Y. Ota, Y. Harada, A. Ebata, M. Moriya, H. Onoda, K. Onogi, H. Kamahori, C. Kobayashi,
699 H. Endo, K. Miyaoka, and K. Takahashi, 2015: The JRA-55 reanalysis: General specifications
700 and basic characteristics, *J. Meteorol. Soc. Jpn.*, **93**, 5-48.

701 Mesinger, F., G. DiMego, E. Kalnay, K. Mitchell, P. C. Shafran, W. Ebisuzaki, D. Jović, J. Woollen, E.
702 Rogers, E. H. Berbery, M. B. Ek, Y. Fan, R. Grumbine, W. Higgins, H. Li, Y. Lin, G. Manikin,
703 D. Parrish, and W. Shi, 2006: North American Regional Reanalysis. *Bull. Amer. Meteor. Soc.*,
704 **87**, 343–360.

705 Mittermaier, M. P., 2014: A strategy for verifying near-convection-resolving model forecasts at
706 observing sites. *Weather and Forecasting*, **29**(2), 185-204.

707 National Centers for Environmental Prediction/National Weather Service/NOAA/U.S. Department of
708 Commerce, 2008: NCEP ADP Global Upper Air and Surface Weather Observations
709 (PREPBUFR format). *Research Data Archive at the National Center for Atmospheric Research*,
710 *Computational and Information Systems Laboratory*, Boulder, CO. [Available online at

711 <https://doi.org/10.5065/Z83F-N512>.] Accessed 5 July 2018.

712 National Climatic Data Center/NESDIS/NOAA/U.S. Department of Commerce, Meteorology
713 Department/Florida State University, Climate Analysis Section/Climate and Global Dynamics
714 Division/National Center for Atmospheric Research/University Corporation for Atmospheric
715 Research, and Harvard College Observatory/Harvard University, 1981: World Monthly Surface
716 Station Climatology. *Research Data Archive at the National Center for Atmospheric Research,*
717 *Computational and Information Systems Laboratory*, Boulder, CO. [Available online at
718 <http://rda.ucar.edu/datasets/ds570.0/>.] Accessed 7 Nov 2019.

719 On, N., H. M. Kim, and S. Kim, 2018: Effects of resolution, cumulus parameterization scheme,
720 and probability forecasting on precipitation forecasts in a high-resolution limited-area
721 ensemble prediction system, *Asia-Pacific Journal of Atmospheric Sciences*, **54**, 623-
722 637, doi:10.1007/s13143-018-0081-4.

723 Onogi, K., J. Tsutsui, H. Koide, M. Sakamoto, S. Kobayashi, H. Hatsushika, T. Matsumoto, N.
724 Yamazaki, H. Kamahori, K. Takahashi, S. Kadokura, K. Wada, K. Kato, R. Oyama, T.
725 Ose, N. Mannoji, and R. Taira, 2007: The JRA-25 reanalysis. *J. Meteor. Soc. Japan*, **85**,
726 369–432.

727 Park, J., and H. M. Kim, 2020: Design and evaluation of CO₂ observation network to optimize surface
728 CO₂ fluxes in Asia using observation system simulation experiments, *Atmospheric Chemistry*
729 *and Physics*, **20**, 5175-5195, <https://doi.org/10.5194/acp-20-5175-2020>.

730 Penny, S. G., 2014: The hybrid local ensemble transform Kalman filter. *Monthly Weather Review*,
731 **142**(6), 2139-2149.

732 Penny, S. G., D. W. Behringer, J. A. Carton, and E. Kalnay, 2015: A hybrid global ocean data
733 assimilation system at NCEP. *Monthly Weather Review*, **143**(11), 4660-4677.

734 Que, L. J., W. L. Que, and J. M. Feng, 2016: Intercomparison of different physics schemes in the WRF
735 model over the Asian summer monsoon region. *Atmospheric and Oceanic Science Letters*, **9**(3),
736 169-177.

737 Renshaw, R., P. Jermey, D. Barker, A. Maycock, and S. Oxley, 2013: EURO4M regional reanalysis
738 system, *Forecasting Research Technical Report*, No. **583**, Met Office.

739 Rienecker, M. M., M. J. Suarez, R. Gelaro, R. Todling, J. Bacmeister, E. Liu, M. G. Bosilovich, S. D.
740 Schubert, L. Takacs, G.-K. Kim, S. Bloom, J. Chen, D. Collins, A. Conaty, A. da Silva, W. Gu,
741 J. Joiner, R. D. Koster, R. Lucchesi, A. Molod, T. Owens, S. Pawson, P. Pegion, C. R. Redder,
742 R. Reichle, F. R. Robertson, A. G. Ruddick, M. Sienkiewicz, and J. Woollen, 2011: MERRA:
743 NASA's Modern-Era Retrospective Analysis for Research and Applications. *J. Climate*, **24**,
744 3624–3648.

745 Saha, S., S. Moorthi, H.-L. Pan, X. Wu, J. Wang, S. Nadiga, P. Tripp, R. Kistler, J. Woollen, D. Behringer,
746 H. Liu, D. Stokes, R. Grumbine, G. Gayno, J. Wang, Y.-T. Hou, H.-Y. Chuang, H.-M. H. Juang,
747 J. Sela, M. Iredell, R. Treadon, D. Kleist, P. V. Delst, D. Keyser, J. Derber, M. Ek, J. Meng, H.
748 Wei, R. Yang, S. Lord, H. V. D. Dool, A. Kumar, W. Wang, C. Long, M. Chelliah, Y. Xue, B.
749 Huang, J.-K. Schemm, W. Ebisuzaki, R. Lin, P. Xie, M. Chen, S. Zhou, W. Higgins, C.-Z. Zou,
750 Q. Liu, Y. Chen, Y. Han, L. Cucurull, R. W. Reynolds, G. Rutledge, and M. Goldberg, 2010: The
751 NCEP Climate Forecast System Reanalysis. *Bull. Amer. Meteor. Soc.*, **91**, 1015–1057.

752 Schubert, S., J. Pfendtner, and R. Rood, 1993: An assimilated dataset for earth science applications.
753 *Bull. Amer. Meteor. Soc.*, **74**, 2331–2342.

754 Shiferaw, A., T. Tadesse, C. Rowe, and R. Oglesby, 2018: Precipitation extremes in dynamically
755 downscaled climate scenarios over the greater horn of Africa. *Atmosphere*, **9**(3), 112.

756 Shin, I.-C, J.-G. Kim, C.-Y. Chung, S.-K. Baek, and J.-R. Lee, 2016: The impact of the COMS data on
757 the KMA NWP System, *14th JCSDA Technical Review Meeting & Science Workshop on*
758 *Satellite Data Assimilation*.

759 Skamarock, W. C., J. B. Klemp, J. Dudhia, D. O. Gill, D. M. Barker, M. G. Duda, X.-Y. Huang, W.
760 Wang, J. G. Powers, 2008: A description of the advanced research WRF version 3. NCAR Tech.
761 Note NCAR/TN-475+ STR Available at:
762 <https://opensky.ucar.edu/islandora/object/technotes%3A500/datastream/PDF/view>.

763 Tewari, M., F. Chen, W. Wang, J. Dudhia, M. A. LeMone, K. Mitchell, M. Ek, G. Gayno, J. Wegiel, and

764 R. H. Cuenca, 2004: Implementation and verification of the unified NOAH land surface model
765 in the WRF model. *20th conference on weather analysis and forecasting/16th conference on*
766 *numerical weather prediction* (Vol. 1115). Seattle, WA: American Meteorological Society.

767 Theis, S. E., A. Hense, and U. Damrath, 2005: Probabilistic precipitation forecasts from a deterministic
768 model: A pragmatic approach. *Meteorological Applications: A journal of forecasting, practical*
769 *applications, training techniques and modelling*, **12**(3), 257-268.

770 Thompson, G., P. R. Field, R. M. Rasmussen, and W. D. Hall, 2008: Explicit forecasts of winter
771 precipitation using an improved bulk microphysics scheme. Part II: Implementation of a new
772 snow parameterization. *Mon. Wea. Rev.*, **136**(12), 5095-5115.

773 Uppala, S. M., P. W. KÅllberg, A. J. Simmons, U. Andrae, V. D. C. Bechtold, M. Fiorino, J. K. Gibson,
774 J. Haseler, A. Hernandez, G. A. Kelly, X. Li, K. Onogi, S. Saarinen, N. Sokka, R. P. Allan, E.
775 Andersson, K. Arpe, M. A. Balmaseda, A. C. M. Beljaars, L. V. D. Berg, J. Bidlot, N. Bormann,
776 S. Caires, F. Chevallier, A. Dethof, M. Dragosavac, M. Fisher, M. Fuentes, S. Hagemann, E.
777 Hólm, B. J. Hoskins, L. Isaksen, P. A. E. M. Janssen, R. Jenne, A. P. McNally, J.-F. Mahfouf, J.-
778 J. Morcrette, N. A. Rayner, R. W. Saunders, P. Simon, A. Sterl, K. E. Trenberth, A. Untch, D.
779 Vasiljevic, P. Viterbo, and J. Woollen, 2005: The ERA-40 re-analysis. *Q. J. R. Meteorol. Soc.*,
780 **131**: 2961–3012.

781 Warrick, F., 2015: Options for filling the LEO-GEO AMV Coverage Gap. *NWP SAF Tech. Doc.*, NWP
782 SAF-MO-TR-030, 21 p.

783 Wilks, D. S., 2006: Statistical methods in the atmospheric sciences, 2nd edn., *Academic Press*, 627pp.

784 Wilson, L., 2010: Verification of severe weather forecasts in support of the “SWFDP Southern Africa”
785 project. *Report for the World Meteorological Organisation*, pp. 21
786 (www.wmo.int/pages/prog/www/BAS/documents/Doc-7-Verification.doc)

787 Yang, E.-G., and H. M. Kim, 2017: Evaluation of a regional reanalysis and ERA-Interim over East Asia
788 using in situ observations during 2013-14, *Journal of Applied Meteorology and*
789 *Climatology*, **56**(10), 2821-2844,

790 Yang, E.-G., and H. M. Kim, 2019: Evaluation of Short-Range Precipitation Reforecasts from East Asia

791 Regional Reanalysis. *Journal of Hydrometeorology*, **20**(2), 319-337.

792 Yang, E.-G., and H. M. Kim, 2021a: A comparison of variational, ensemble-based, and hybrid data
793 assimilation methods over East Asia for two one-month periods, *Atmospheric Research*, **249**,
794 105257.

795 Yang, E.-G., and H. M. Kim, 2021b: East Asia Regional Reanalysis 6 hourly data on pressure levels
796 from 2010 to 2019, <https://doi.org/10.7910/DVN/7P8MZT>, Harvard Dataverse, V1.

797 Yang, E.-G., and H. M. Kim, 2021c: East Asia Regional Reanalysis 6 hourly precipitation data from
798 2010 to 2019, <https://doi.org/10.7910/DVN/Q07VRC>, Harvard Dataverse, V1.

799 Yoo, C., and E. Cho, 2018: Comparison of GCM precipitation predictions with their RMSEs and pattern
800 correlation coefficients. *Water*, **10**(1), 28.

801 Zhang, F., M. Zhang, and J. Poterjoy, 2013: E3DVar: Coupling an ensemble Kalman filter with three-
802 dimensional variational data assimilation in a limited-area weather prediction model and
803 comparison to E4DVar. *Monthly Weather Review*, **141**(3), 900-917.

804 Zhang, Q., Y. Pan, S. Wang, J. Xu, and J. Tang, 2017: High-resolution regional reanalysis in China:
805 Evaluation of 1 year period experiments. *Journal of Geophysical Research: Atmospheres*,
806 **122**(20), 10-801.

807

808 **Table caption**

809 Table 1. Model configuration.

810 Table 2. Summary of observations used in this study. The default observation error statistics
811 provided in WRFDA system are used for assimilation in this study. The variables u , v , T , RH ,
812 P_s , and TPW denote zonal wind, meridional wind, temperature, relative humidity, surface
813 pressure, and total precipitable water, respectively.

814 Table 3. (Re)analyses and (re)forecasts and corresponding experiments used in this study.

815 Table 4. The 2×2 contingency table for dichotomous (yes-no) events.

816

817 **Figure caption**

818 Figure 1. The East Asia Regional Reanalysis domain ~~with different types of NCEP PrepBUFR~~
819 ~~observations available for assimilation at 00 UTC on 1st of January in 2017~~. The black dashed
820 box denotes a verification area. Different types of NCEP PrepBUFR observations are available
821 for assimilation at 00 UTC on 1st of January in 2017.

822 Figure 2. The schematic diagram of the advanced hybrid gain data assimilation method in the
823 East Asia regional reanalysis system.

824 Figure 3. RMSEs of analysis of (a,b) zonal wind, (c,d) meridional wind, (e,f) temperature, and
825 (g,h) Qvapor (water vapor mixing ratio) from ERA-I (black dashed), ERA5 (black solid),
826 E3DVAR (blue dashed), AdvHG (blue solid) depending on pressure levels for (left) January
827 and (right) July in 2017.

828 Figure 4. Same as Fig. 3 except for 24 h forecast.

829 Figure 5. Same as Fig. 3 except for 36 h forecast.

830 Figure 6. RMSEs of analysis of (a) zonal wind, (b) meridional wind, (c) temperature, and (d)
831 Qvapor (water vapor mixing ratio) from ERA5 (black solid) and AdvHG (blue solid) and
832 spreads of analysis (black dashed) and 6 h forecast (gray dashed) of AdvHG depending on
833 pressure levels averaged over the ten-year period of 2010-2019.

834 Figure 7. Same as Fig. 6 except for RMSE of 24 h forecast.

835 Figure 8. (a,c) ETS and (b,d) FBI for (a,b) January and (c,d) July in 2017 depending on
836 thresholds 0.5, 1, 4, 8, and 16 mm (6 h)⁻¹.

837 Figure 9. (a,c) POD and (b,d) FAR for (a,b) January and (c,d) July in 2017 depending on
838 thresholds 0.5, 1, 4, 8, and 16 mm (6 h)⁻¹.

839 Figure 10. Brier skill score of the probabilistic postprocessed forecast with reference to the
840 WRF-based ERA-I for (a-d) January and (e-h) July in 2017 (Blue solid: AdvHG, blue dashed:
841 E3DVAR, red solid: WRF-based ERA5).

842 Figure 11. The spatial distribution of 6 h accumulated precipitation of (1st column) observation,
843 (2nd column) E3DVAR, (3rd column) AdvHG, (4th column) ERA-I, (5th column) ERA5, (6th
844 column) ERA-I_fromECMWF, and (7th column) ERA5_fromECMWF and the pattern
845 correlation coefficient (PCC) shown at the bottom right of each figure at valid time (1st low, 3rd
846 low) 06 UTC and (2nd low, 4th low) 18 UTC on 29th and 30th of January in 2017.

847 Figure 12. As in Fig. 11, but for 1st and 2nd of July in 2017.

848 Figure 13. The spatial distribution of the monthly accumulated precipitation of (a) observations,
849 (b) E3DVAR, (c) AdvHG, (d) ERA-I, (e) ERA5, (f) ERA-I from ECMWF, and (g) ERA5 from
850 ECMWF for January 2017.

851 Figure 14. As in Fig. 13, but for July 2017.

852

853 Table 1. Model configuration

	Description
Hori. Resol.	12 km (540×432 grid points)
Vert. Lev.	50 vertical levels (up to 5 hPa)
Model	WRF Model (v3.7.1, Skamarock et al. 2008)
LBC	ERA5 (Hersbach et al. 2020)
Data assimilation	E3DVAR (Zhang et al. 2013), Advanced hybrid gain method
Microphysics	Thompson scheme (Thompson et al. 2008)
Cumulus convection	Grell–Freitas ensemble scheme (Grell and Freitas 2014)
PBL	Yonsei University scheme (Hong et al. 2006)
Radiation	Rapid Radiative Transfer Model (RRTMG) scheme (Iacono et al. 2008)
Surface layer	Revised MM5 Monin-Obukhov scheme (Jiménez et al. 2012)
Surface model	Unified Noah Land Surface Model (Tewari et al. 2004)

854

855

856 Table 2. Summary of observations used in this study. The default observation error statistics
 857 provided in WRFDA system are used for assimilation in this study. The variables u, v, T, RH,
 858 Ps, and TPW denote zonal wind, meridional wind, temperature, relative humidity, surface
 859 pressure, and total precipitable water, respectively.

Observations	Descriptions	Variables	Observation errors (depending on vertical levels)
SOUND	Upper-air observation from radiosonde	u, v	1.1-3.3 m/s
		T	1 K
		RH	10-15%
PROFILER	Upper-air wind profile from wind profiler	u, v	2.2-3.2 m/s
PILOT	Upper-air wind profile from pilot balloon or radiosonde	u, v	2.2-3.2 m/s
AIREP	Upper-air wind and temperature from aircraft	u, v	3.6 m/s
		T	1 K
Scatwind	Scatterometer oceanic surface winds	u, v	2.5-3.8 m/s
SHIPS	Surface synoptic observation from ship	u, v	1.1 m/s
		T	2 K
		Ps	1.6 hPa
		RH	10%
SYNOP	Surface synoptic observation from land station	u, v	1.1 m/s
		T	2 K
		Ps	1 hPa
		RH	10%
BUOY	Surface synoptic observation from buoy	u, v	1.4-1.6 m/s
		T	2 K
		Ps	0.9-1 hPa
		RH	10%
GPSPW	Precipitable water vapor from global positioning system (GPS)	TPW	0.2 mm
METAR	Aviation routine weather report from automatic weather station (AWS)	u, v	1.1 m/s
		T	2 K
		Ps	1 hPa
		RH	10%
AMV	Conventional atmospheric motion vector data from geostationary satellites	u, v	2.5-4.5 m/s

860

861

862

863 Table 3. (Re)analyses and (re)forecasts and corresponding experiments used in this study.

Experiment	(Re)analysis_ <u>(initial condition)</u>	(Re)forecast	<u>(Re)forecast horizontal resolution (km)</u>	<u>Initial time</u>	<u>Boundary condition in WRF</u>
AdvHG (EARR)	Reanalysis from AdvHG	Generated using WRF	<u>12</u>	<u>00/06/ 12/18 UTC</u>	<u>ERA5</u>
E3DVAR	Analysis from E3DVAR	Generated using WRF	<u>12</u>		
WRF-based ERA5	Reanalysis from ERA5	Generated using WRF	<u>12</u>		
WRF-based ERA-I	Reanalysis from ERA-I	Generated using WRF	<u>12</u>		
ERA5_fromECMWF	Reanalysis from ERA5	Downloaded from ECMWF	<u>31</u>		<u>N/A</u>
ERA-I_fromECMWF	Reanalysis from ERA-I	Downloaded from ECMWF	<u>79</u>		

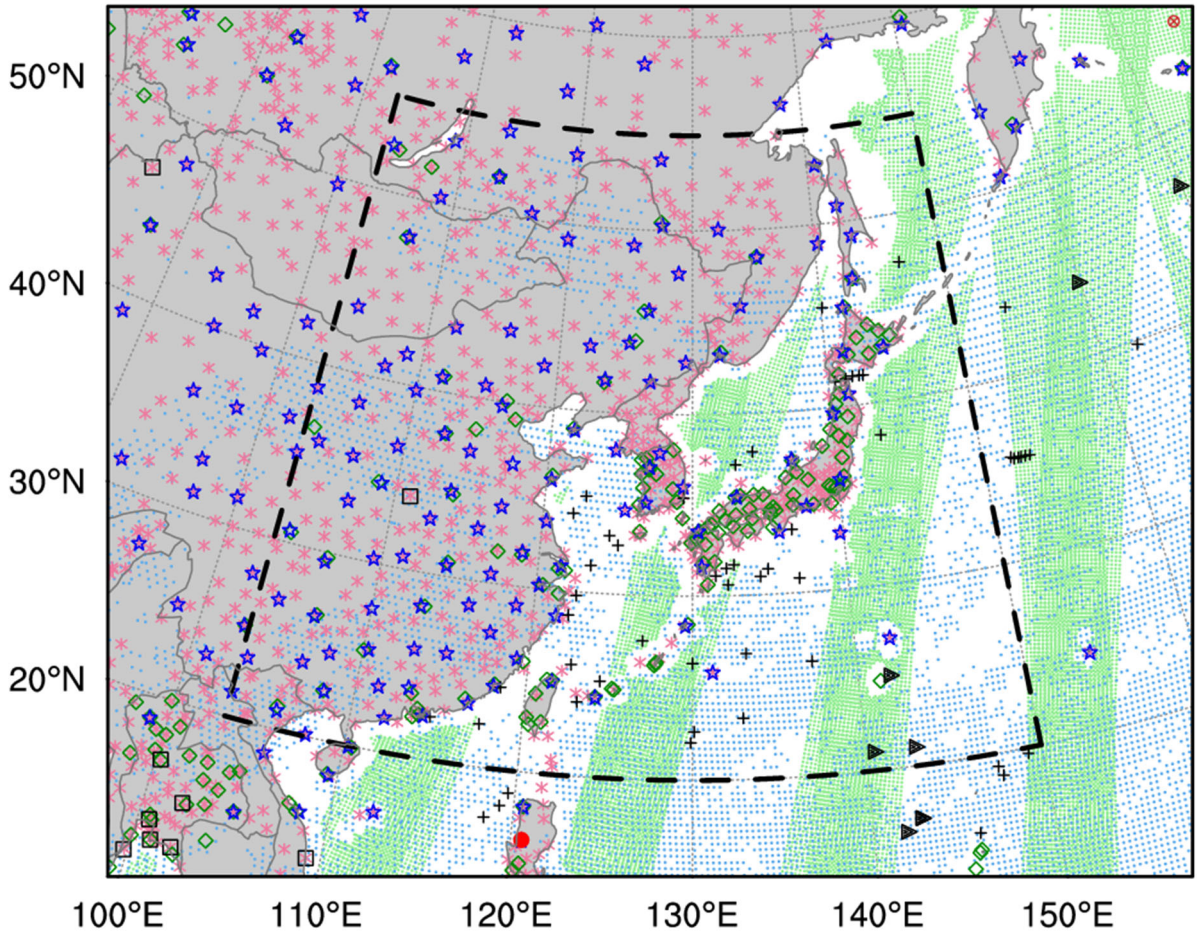
864

865 Table 4. The 2×2 contingency table for dichotomous (yes-no) events.

Forecast	Observed		
	Yes	No	
Yes	Hits (A)	False alarms (B)	A + B
No	Misses (C)	Correct rejections (D)	C + D
	A + C	B + D	Total = A + B + C + D

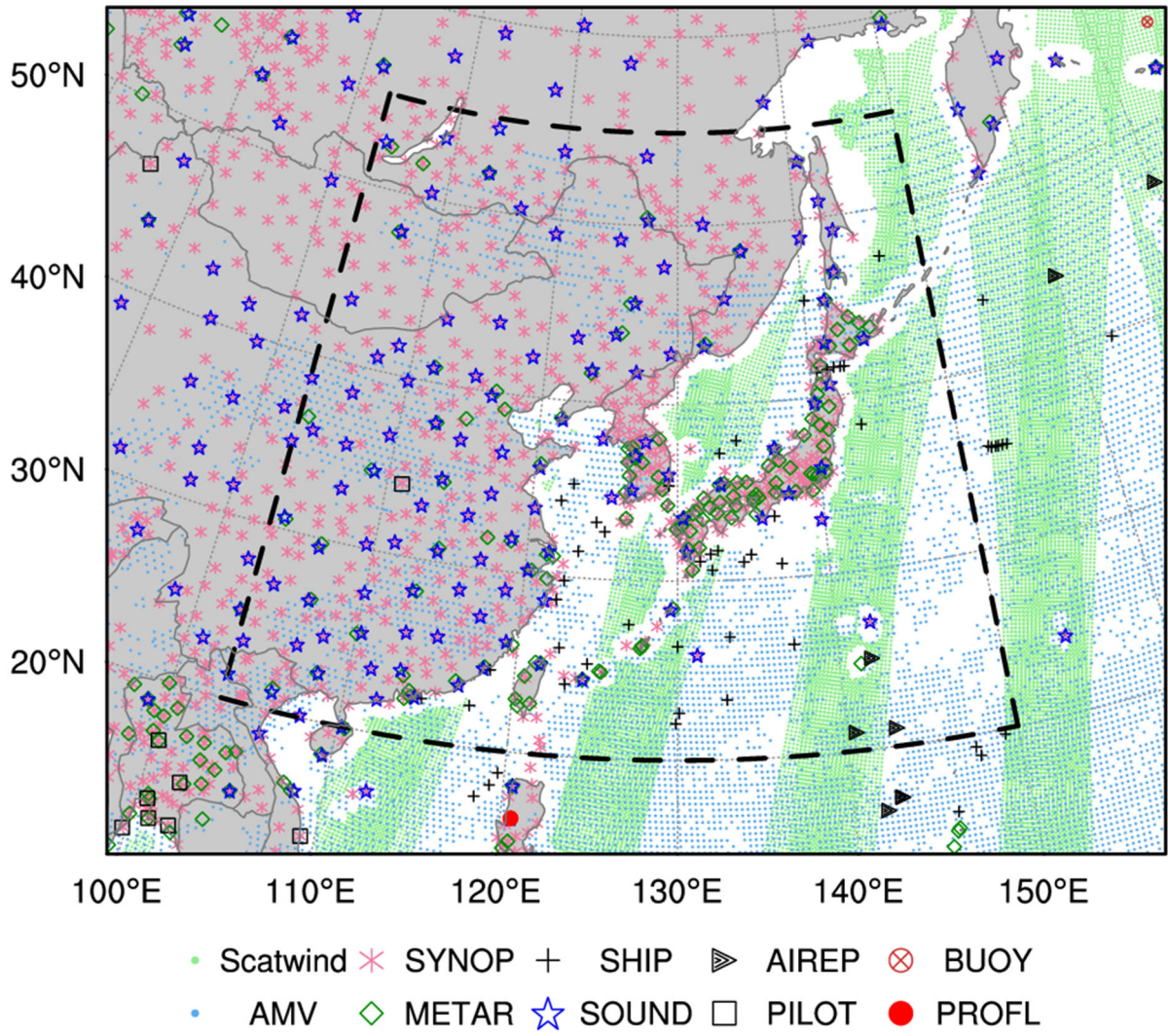
866

2017010100



- Scatwind
- AMV
- * SYNOP
- ◇ METAR
- + SHIP
- ☆ SOUND
- ▴ AIREP
- PILOT
- ⊗ BUOY
- PROFL

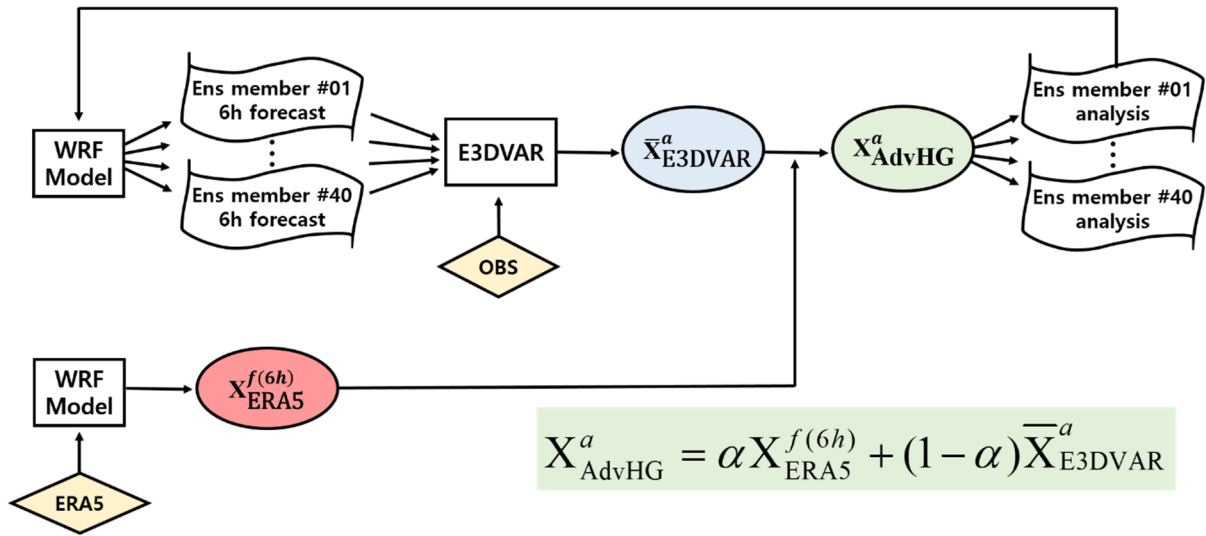
867



868

869 Figure 1. The East Asia Regional Reanalysis domain with different types of NCEP PrepBUFR
 870 observations available for assimilation at 00 UTC on 1st of January in 2017. The black dashed
 871 box denotes a verification area. Different types of NCEP PrepBUFR observations are available
 872 for assimilation at 00 UTC on 1st of January in 2017.

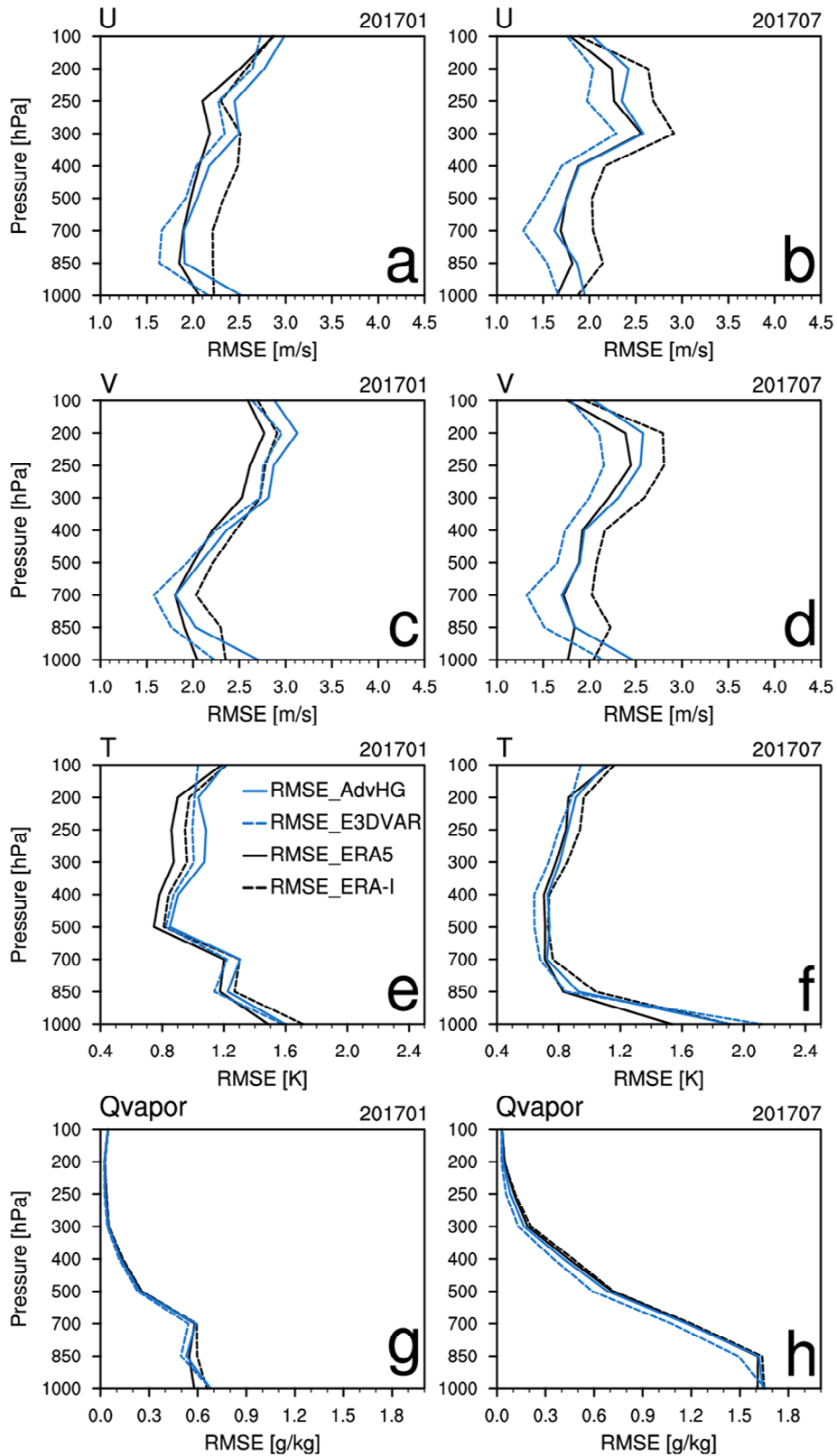
873



874

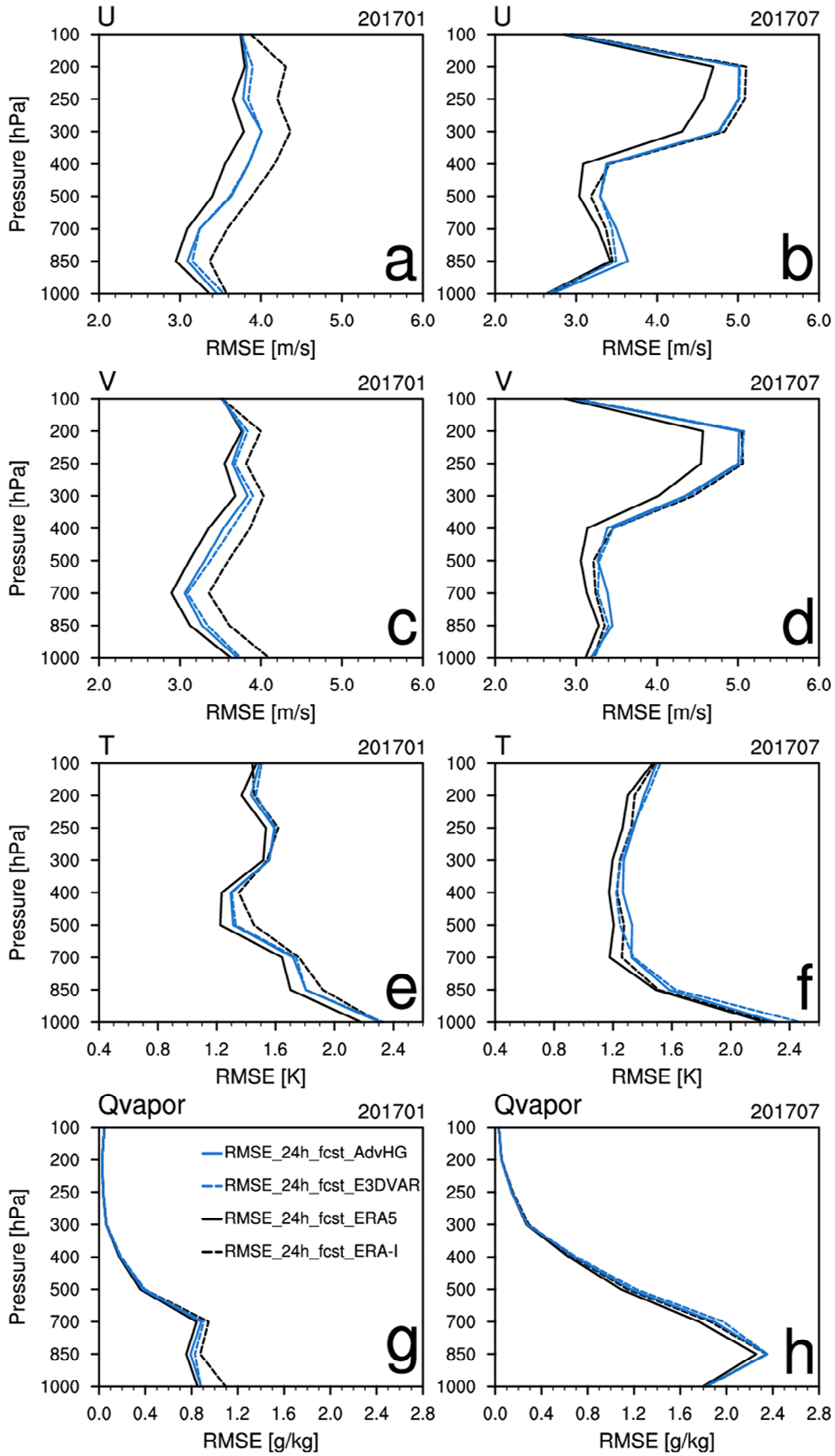
875 Figure 2. The schematic diagram of the advanced hybrid gain data assimilation method in the
 876 East Asia regional reanalysis system.

877



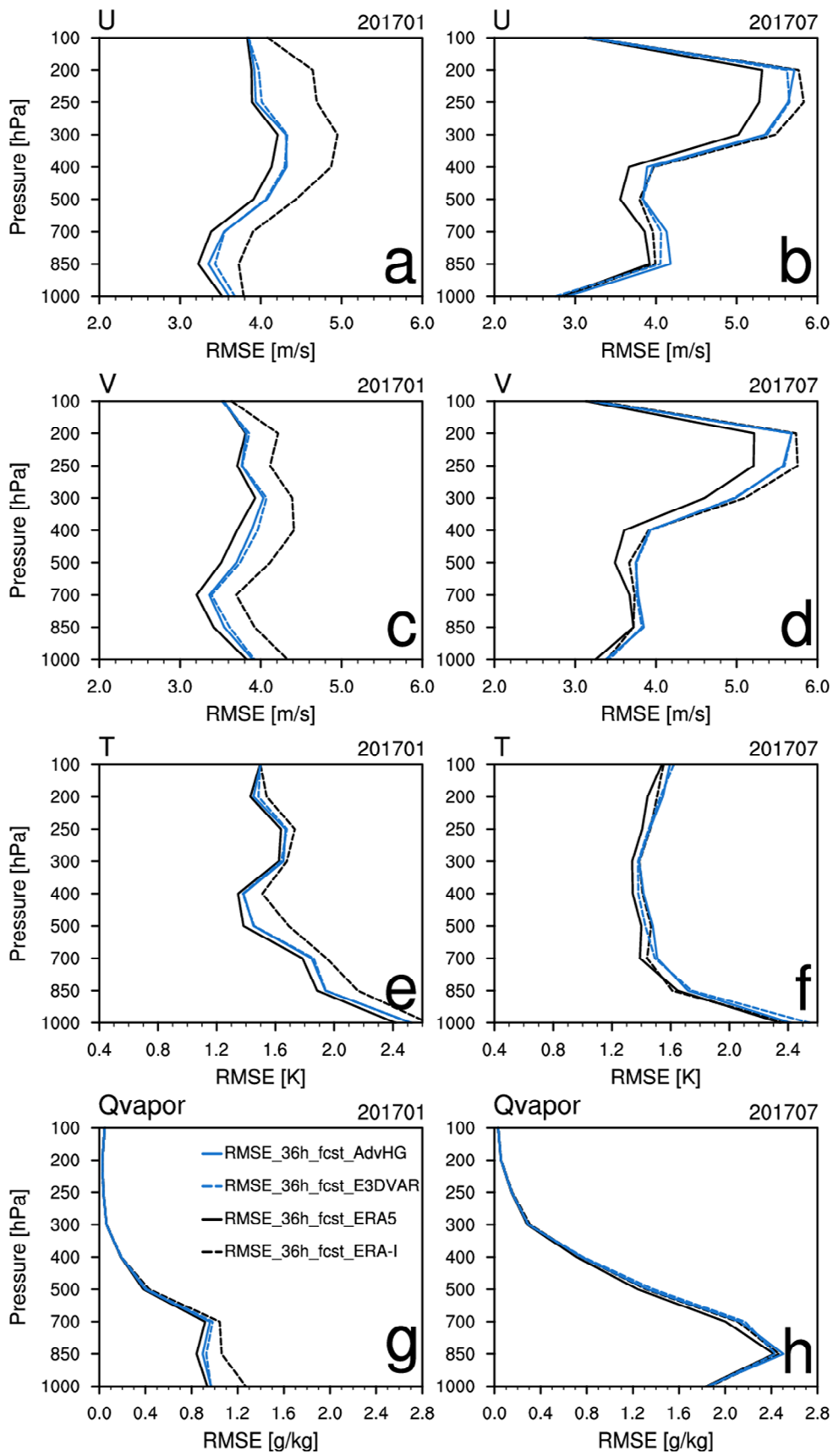
878

879 Figure 3. RMSEs of analysis of (a,b) zonal wind, (c,d) meridional wind, (e,f) temperature, and
 880 (g,h) Qvapor (water vapor mixing ratio) from ERA-I (black dashed), ERA5 (black solid),
 881 E3DVAR (blue dashed), AdvHG (blue solid) depending on pressure levels for (left) January
 882 and (right) July in 2017.



883

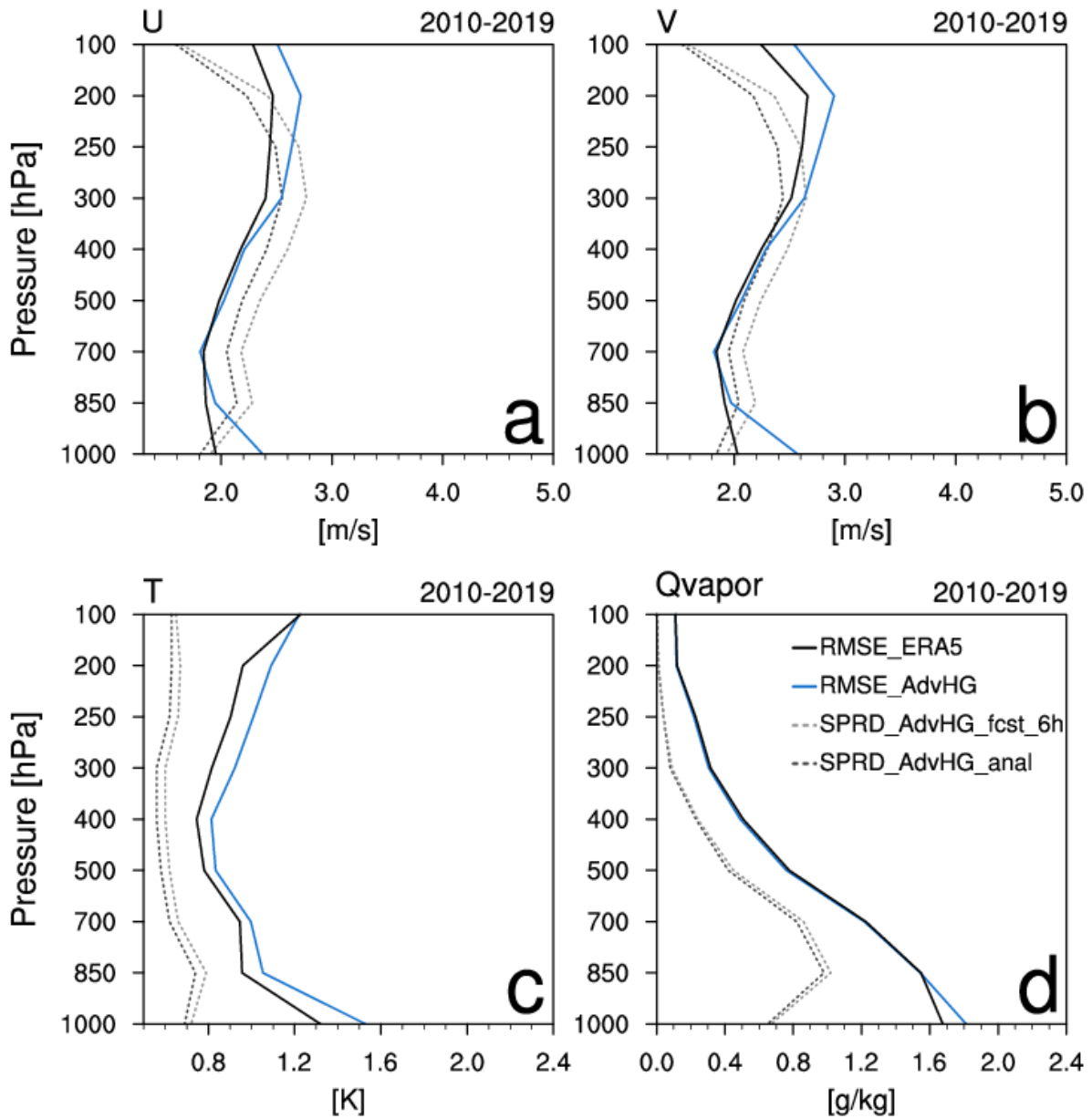
884 Figure 4. Same as Fig. 3 except for 24 h forecast.



885

886 Figure 5. Same as Fig. 3 except for 36 h forecast.

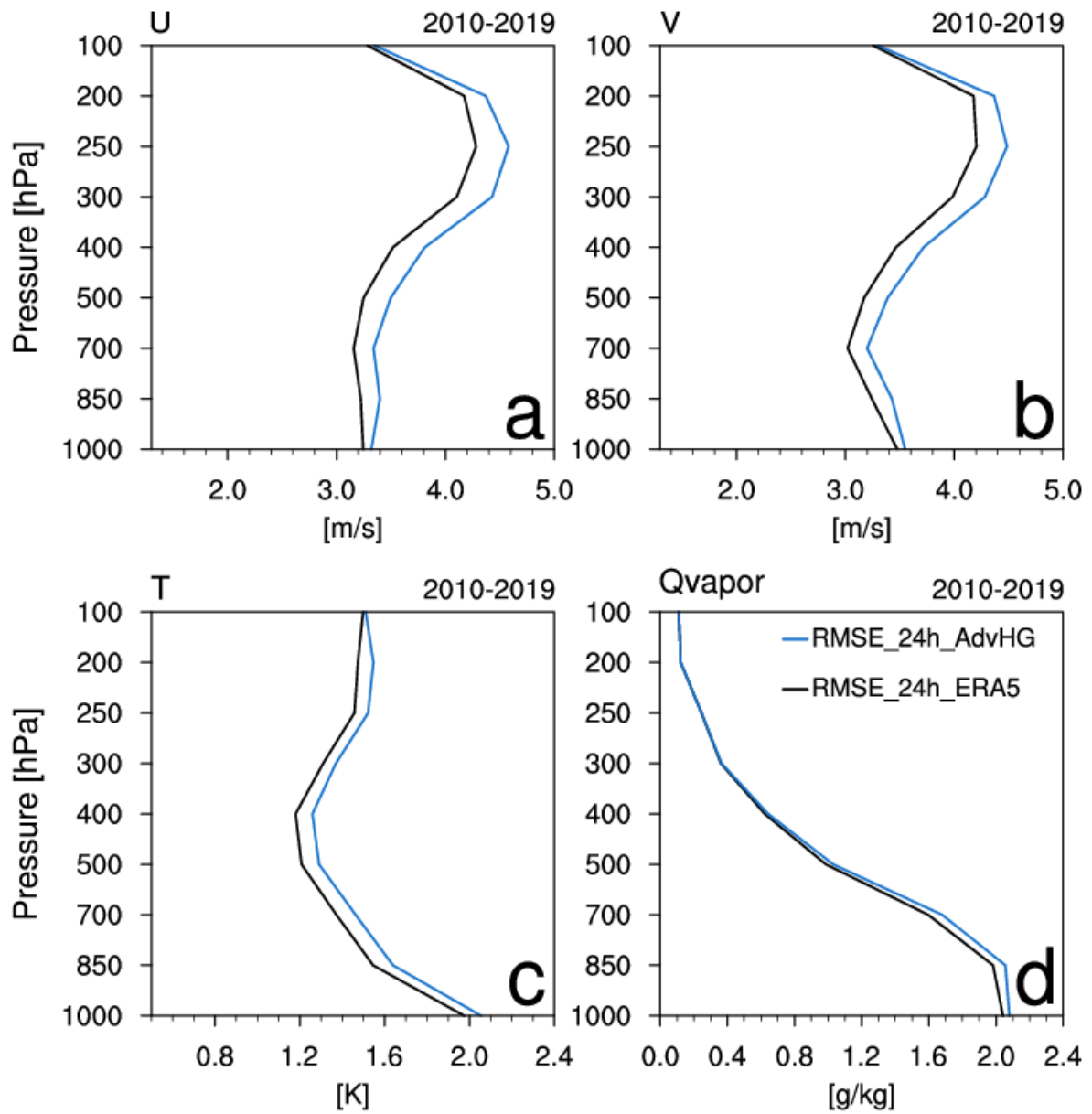
887



888

889 Figure 6. RMSEs of analysis of (a) zonal wind, (b) meridional wind, (c) temperature, and (d)
 890 Qvapor (water vapor mixing ratio) from ERA5 (black solid) and AdvHG (blue solid) and
 891 spreads of analysis (black dashed) and 6 h forecast (gray dashed) of AdvHG depending on
 892 pressure levels averaged over the ten-year period of 2010–2019.

893

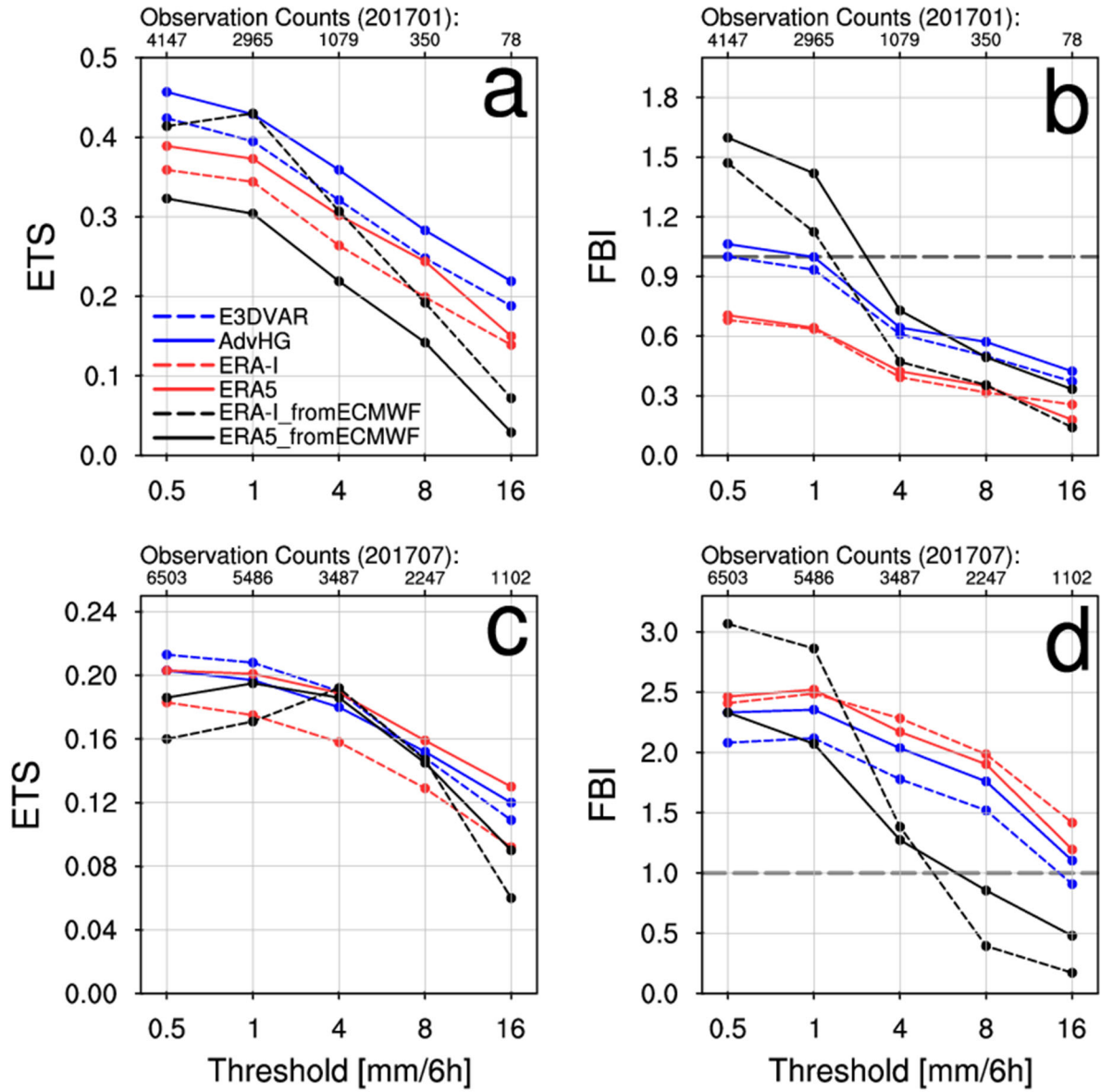


894

895 Figure 7. Same as Fig. 6 except for RMSE of 24 h forecast.

896

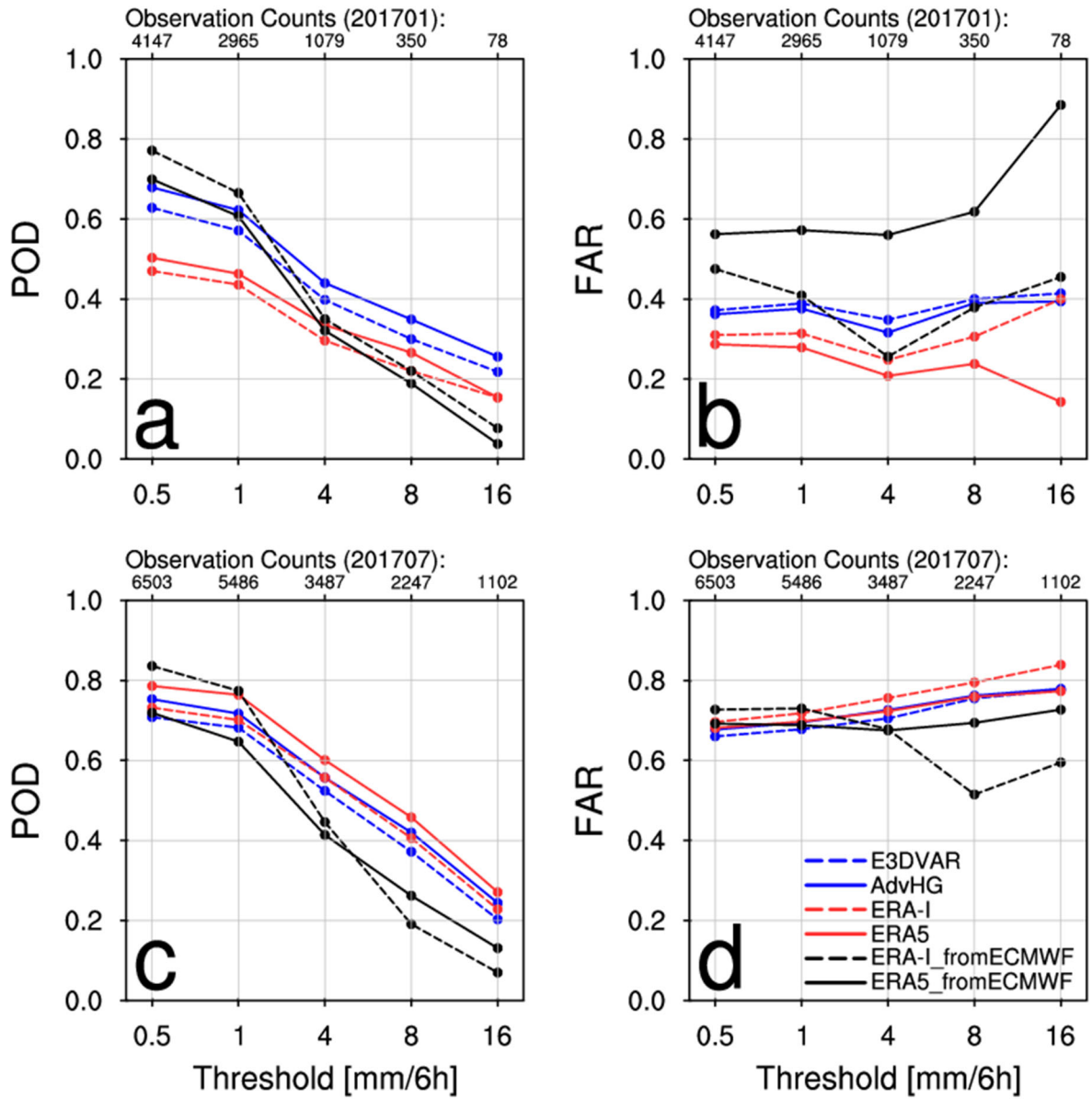
897



898

899 Figure 8. (a,c) ETS and (b,d) FBI for (a,b) January and (c,d) July in 2017 depending on
 900 thresholds 0.5, 1, 4, 8, and 16 mm (6 h)⁻¹.

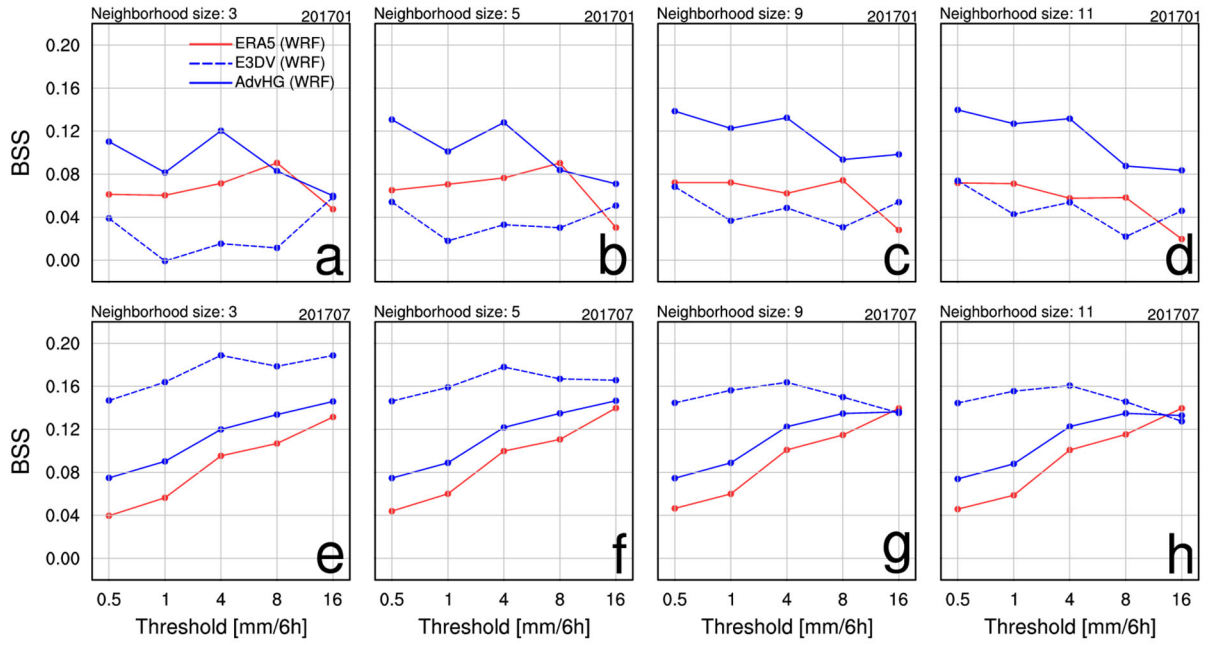
901



902

903 Figure 9. (a,c) POD and (b,d) FAR for (a,b) January and (c,d) July in 2017 depending on
 904 thresholds 0.5, 1, 4, 8, and 16 mm (6 h)⁻¹.

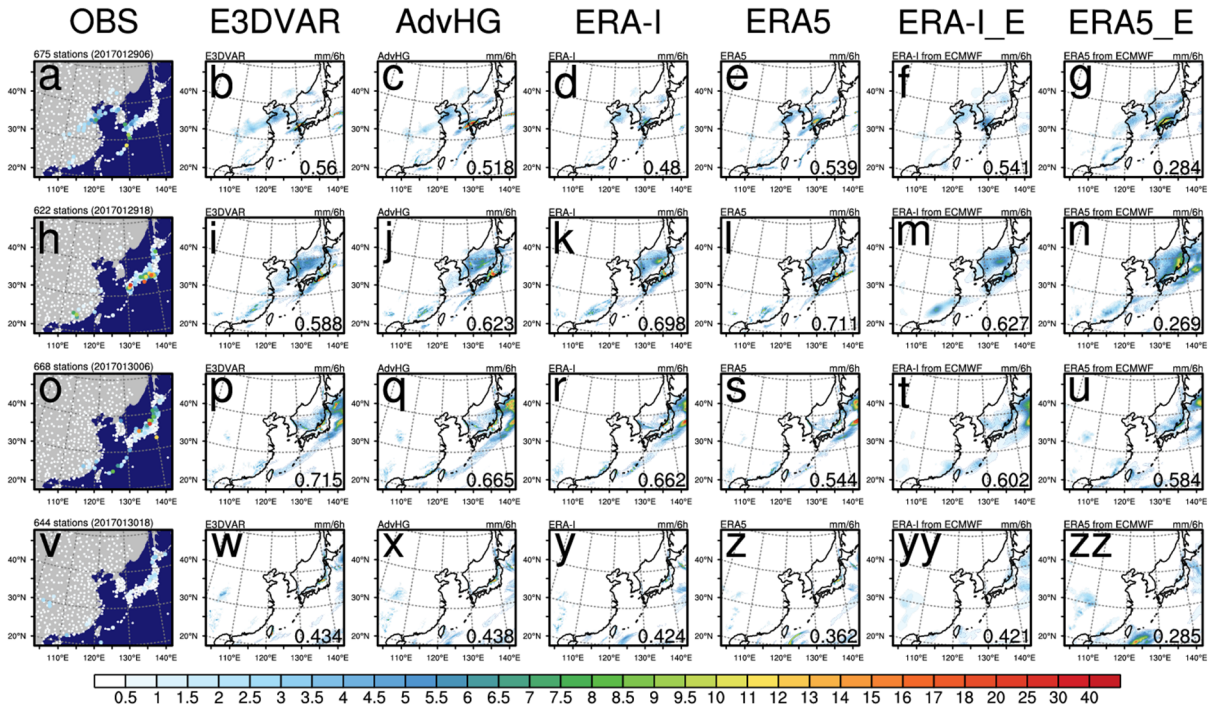
905



906

907 Figure 10. Brier skill score of the probabilistic postprocessed forecast with reference to the
 908 WRF-based ERA-I for (a-d) January and (e-h) July in 2017 (Blue solid: AdvHG, blue dashed:
 909 E3DVAR, red solid: WRF-based ERA5).

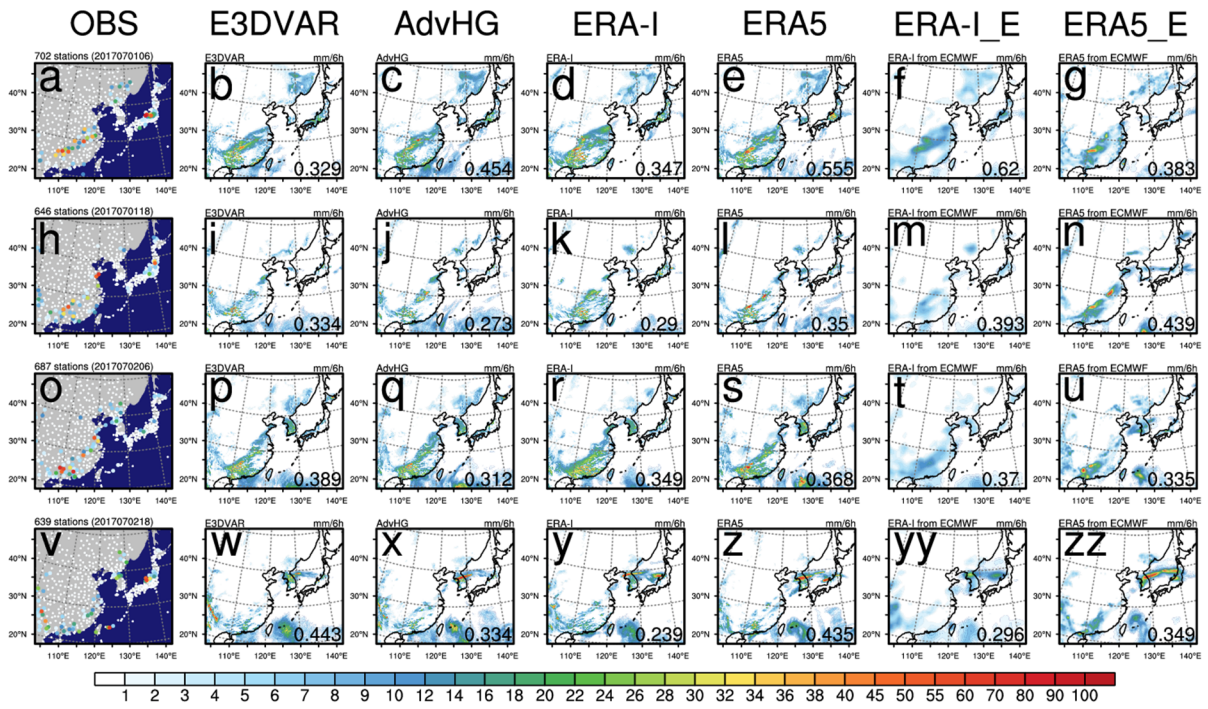
910



911

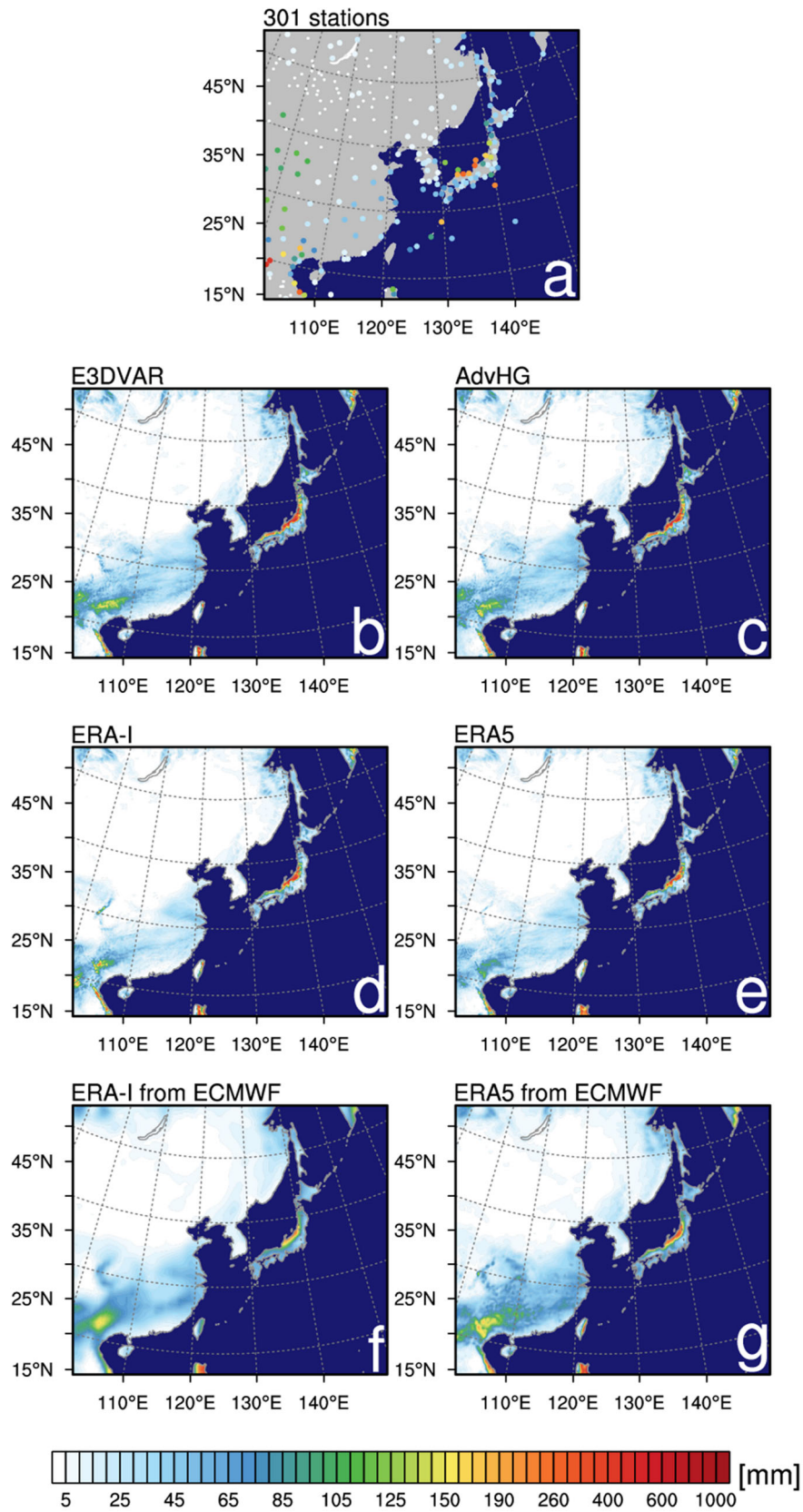
912 Figure 11. The spatial distribution of 6 h accumulated precipitation of (1st column) observation,
 913 (2nd column) E3DVAR, (3rd column) AdvHG, (4th column) ERA-I, (5th column) ERA5, (6th
 914 column) ERA-I_fromECMWF, and (7th column) ERA5_fromECMWF and the pattern
 915 correlation coefficient (PCC) shown at the bottom right of each figure at valid time (1st low, 3rd
 916 low) 06 UTC and (2nd low, 4th low) 18 UTC on 29th and 30th of January in 2017.

917



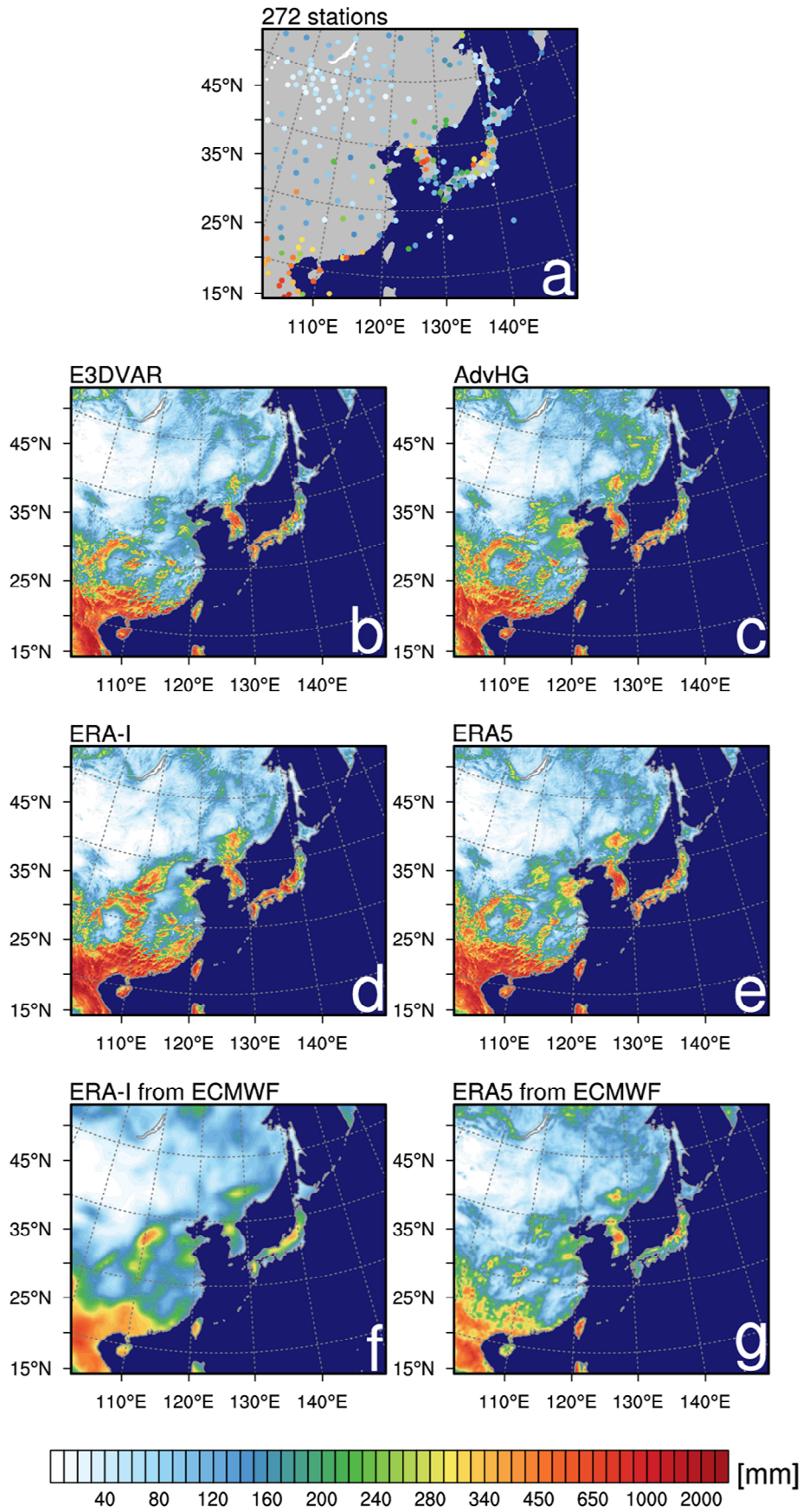
918

919 Figure 12. As in Fig. 11, but for 1st and 2nd of July in 2017.



920

921 Figure 13. The spatial distribution of the monthly accumulated precipitation of (a) observations,
 922 (b) E3DVAR, (c) AdvHG, (d) ERA-I, (e) ERA5, (f) ERA-I from ECMWF, and (g) ERA5 from
 923 ECMWF for January 2017.



924

925 Figure 14. As in Fig. 13, but for July 2017.